Tactile Elastography

Yichen Xiang, Lifeng Zhu, *Member, IEEE*, Aiguo Song, *Senior Member, IEEE*, and Yongjie Jessica Zhang

***Abstract*—Elasticity is one of the representative parameters that reflect the mechanical properties of soft materials. Detecting the underneath elasticity distribution called elastography is a key step for understanding and interacting with objects. Existing solutions for capturing the interior elasticity distribution typically rely on expensive apparatus. In this work, the dense tactile signal captured by the high-resolution vision-based tactile sensor is introduced as a new modality for reconstructing 3-D elasticity distribution. We propose a model-based method, which exploits the tactile maps from active pressing trials for the elastography task. The interior elasticity distribution for nonrigid objects is reconstructed from an inverse physics model. We analyze the credibility of the estimated elasticity distribution obtained from our method. Varying design factors are also discussed. We experiment our method on a set of synthesized 3-D models and physical models in robot-assisted scenes. Various experimental results have been gathered, demonstrating the efficacy of our approach in perceiving elasticity distribution.**

***Index Terms*—Force and tactile sensing, object detection, segmentation and categorization, soft sensors and actuators, vision-based tactile perception.**

Nomenclature

Variables and Definitions

Symbol	Meaning.
$\mathbf{e}^*$	Initial guess of the object's elasticity distribution.
$\mathbf{e}_{\text{gt}}$	Ground-truth elasticity distribution of the object.
$\hat{\mathbf{e}}$	Estimated elasticity distribution of the object.
$\hat{\mathbf{u}}$	Predicted nodal displacements of the object.
$\mathbf{u}, \mathbf{e}$	Nodal displacements and elasticity distribution of the object.
$\mathbf{u}_o, \mathbf{f}_o$	Observable nodal displacements and nodal forces on the object.
$\mathbf{u}_s, \mathbf{f}_s, \mathbf{e}_s$	Nodal displacements, nodal forces and elasticity distribution of the sensor.
$\mathbf{F}$	Deformation gradient.
λ, μ	Lame constants.
$\mathbf{A}^{(i)}$	Constraint matrix for boundary condition in the ith sampling with the stiffness of a zero-length spring.
$\mathbf{S}^{(i)}$	Selection matrix for touching points in the ith sampling.
n, m	Number of object's nodes and elements.
n_s, m_s	Number of sensor's nodes and elements.
n_c	Number of contact nodes on the object surface.

Received 17 January 2025; revised 17 March 2025; accepted 24 April 2025. Date of publication 6 June 2025; date of current version 23 June 2025. This work was supported in part by the National Key Technologies R&D Program under Grant 2024YFB4708802, in part by the NSFC under Grant 62133009 and Grant 92148205, in part by the Natural Science Foundation of Jiangsu Province Major Project under Grant BK20232008, in part by the Jiangsu Key Research and Development Plan under Grant BE2023023-4, in part by the Fundamental Research Funds for the Central Universities. This article was recommended for publication by Associate Editor V. Ho and Editor A. Menciassi upon evaluation of the reviewers' comments. *(Corresponding author: Lifeng Zhu.)*

This work involved human subjects or animals in its research. Approval of all ethical and experimental procedures and protocols was granted by the IEC for Clinical Research of Zhongda Hospital, Affiliated to Southeast University (under Application No. 2023ZDSYLL343-P01, and performed in line with the Declaration of Helsinki (2013), the CIOMS International Ethical Guidelines (2016), and relevant Chinese regulatory standards).

Yichen Xiang, Lifeng Zhu, and Aiguo Song are with the State Key Laboratory of Digital Medical Engineering, Jiangsu Key Lab of Robot Sensing and Control, School of Instrument Science and Engineering, Southeast University, Nanjing 210096, China (e-mail: 230239001@seu.edu.cn; lifengzhu@seu.edu.cn; a.g.song@seu.edu.cn).

Yongjie Jessica Zhang is with the Computational Bio-modeling Laboratory, Department of Mechanical Engineering, Carnegie Mellon University, Pittsburgh, PA 15213 USA (e-mail: jessicaz@andrew.cmu.edu).

This article has supplementary downloadable material available at https://doi.org/10.1109/TRO.2025.3577024, provided by the authors.

Digital Object Identifier 10.1109/TRO.2025.3577024

I. Introduction

INSPECTING underneath material distribution is a long-awaited ability for humans. Since the invention of computer tomography, magnetic resonance imaging, ultrasound, and other imaging techniques, humans have been able to observe the internal structures of various objects without destroying them. Many medical and industrial applications are promoted, significantly benefiting human life. However, precise imaging of the internal 3-D field is at the cost of expensive and bulky instruments, which are not easily accessible to the population and we are still in search of new imaging modalities.

On the other side, humans are able to perceive the internal structures of soft objects without using expensive equipment. For example, experienced doctors could estimate the lumps inside the skin by actively touching the soft tissue with their fingers. During the palpation process, they might even feel its hardness and decide whether further treatment is required from their expertise. Inspired by the manual palpation, we will explore whether robots could also understand the haptic information for imaging the interior distribution of soft matters.

Robot-assisted palpation has been studied in the literature. Researchers proposed to utilize the haptic and proprioceptive information by probing soft materials for lump detection [1], [2], [3], [4], [5], [6]. While positive statistics are reported, the results are dependent on the collected training data, which probably overfit to the tested phantom model. In addition, the goal of lump detection or localization is also far from the imaging task. The task of lump detection only provides boolean or rough low-dimensional vector information of the position and scale of the lump, but imaging aims to generate a rich field of the material distribution.

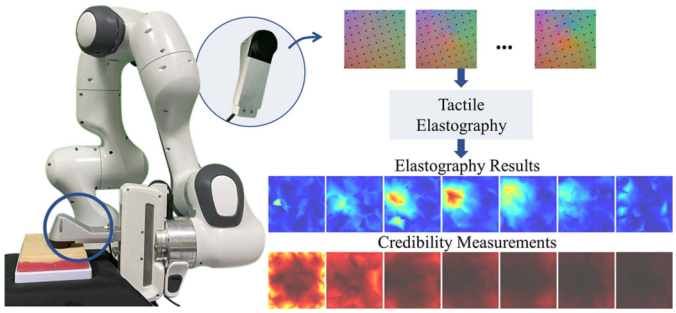

Fig. 1. Proposed robot-assisted tactile elastography leverages tactile information to image the invisible 3-D interior elasticity distribution. A physics model is adopted to estimate the stiffness distribution within the skin and provide credibility for the elastography measurements.

While it seems difficult to recover the 3-D distribution of soft materials, we note that the deformation of soft objects depends on their material distribution. It is verified that the constitutive material could be estimated from captured deformation [7], [8], which is assumed visually available in simulated environments. Various interior characteristics cause different extrinsic responses to the same stimulation, allowing us to infer them from the extrinsic information. This idea follows the concept of "elastography," which has been recognized in ultrasound imaging. The density field, which is also related to the elastic property of the object, causes different responses to the ultrasound stimulation [9]. Therefore, we may estimate and plot the distribution of elastic material from ultrasounds, producing elastography thereafter. In this work, following a similar approach to estimating material distribution from elastic behavior, we aim to exploit heuristic data in palpation. Our goal is to study the mapping of proprioceptive and haptic information to the 3-D material distribution.

Recent advances in tactile sensor development also shed light on our task. Traditionally, it is not effective to infer the rich 3-D material distribution from low-dimensional force signals. Recently, tactile information with high spatial resolution has become available with the miniaturization of tactile sensors [10], [11] and the popularization of vision-based tactile techniques [12]. By installing them on robotic manipulators, we expect to extract versatile signals to facilitate the recovery of material distribution.

In this work, as our goal is to image the 3-D material distribution from the tactile information collected in palpation, we will call our work "tactile elastography" throughout the article. Fig. 1 provides a visual overview of our system. We actively press the target object with a tactile sensor and sample tactile images as the input of tactile elastography. We build an inverse physics model to study the elastic material in terms of the distribution of Young's modulus, to fit the acquired tactile signals. We analyze the sensitivity of our model to provide credibility measurements of the elastography results. Our method is experimented with various configurations in a simulated environment and tested using vision-based tactile sensors on real-world soft objects. As an application of our system, we also show the advantages of our imaging technique compared to learning-based solutions for lump detection using robot-assisted palpation. The key contribution of our work can be summarized as follows.

1) Dense vision-based tactile information with higher spatial acuity is introduced for estimating the interior elasticity distribution of nonrigid objects.
2) A model-based solution is developed for elastography from tactile signals with its credibility analyzed.
3) Our method is experimented with different cases and potential applications in robot-assisted palpation are proposed.

II. Related Work

A. Elastography

As an elasticity imaging approach, elastography is developed to display elasticity distribution in soft tissues. Typical solutions such as mechanical imaging (MI), ultrasonic elastography (USE), magnetic resonance elastography (MRE), and optical coherence elastography (OCE) have been developed. USE, MRE, and OCE methods were developed based on current ultrasonic imaging [3], [13], [14], [15], magnetic resonance imaging [16], [17], and optical coherence tomography [18], which could be based on static [19], [20] or dynamic methods [21]. The MI devices for elasticity imaging were described in the literature [22], [23], [24], which provided an alternative semiempirical way of 3-D image formation. Most elastography methods, regardless of the modality, share a common framework consisting of a stimulation device, a receiver, and an inverse solver. These methods rely on various modalities, including ultrasound, optical waves, force, or magnetic fields. In this article, we aim to investigate the response of materials using a new modality, tactile, and explore its potential for revealing the interior distribution of materials. Unlike conventional imaging modalities that require expensive equipment, tactile data is more accessible, thanks to advances in tactile sensors introduced by the robotics community.

Researchers also tried to perceive the object tissue purely through mechanical signals such as force and surface deformation using physics-based algorithms. Sangpradit et al. [4] proposed a tumor localization method using rolling indentation based on inverse finite element analysis. However, it only allowed the detection of the tumor position when its material properties were known or estimated the tumor elasticity when its location was given. Olson et al. [25] proposed a system to automate the manual breast exam process and generated a binary stiffness map of the breast with a bulky mechanical device. Differently, we propose to exploit the power of light tactile sensors for continuously estimating the elasticity distribution.

Mapping the material properties is also one task in computer vision. Material properties were designed to fit the desired animation captured as point clouds [26] or reproduce the target forces [27]. Researchers also proposed to work with the vibration captured from videos for estimating the object material [7], [8]. However, the vision-based methods are susceptible to environmental light and materials interference. In contrast, tactile information directly measures the material's response through physical contact with the object, making it independent of lighting conditions. This allows tactile sensors to capture data even in challenging environments, such as those with poor

lighting or highly reflective surfaces, where vision-based methods may encounter significant interference. In this article, we will study the tactile information for elastography to avoid these problems.

B. Vision-Based Tactile Sensor

Vision-based tactile sensors have emerged as a novel fingertip in robot touch for their high spatial resolution and abundant outputs [12]. Based on these sensors, various tasks of estimating the material properties have been reported. For instance, physics-driven and data-driven approaches for estimating liquid properties, such as height [28] and viscosity [29], have been proposed through grasp manipulation with vision-based sensors. Except for liquid properties, hardness [30] and texture [31] can also be computed to assist robots in recognizing and distinguishing objects.

Jia et al. [32] evaluated the perception sensitivity of the vision-based tactile system for inclusions by observing the hump that forms over the inclusions. They concluded that the Gelsight sensor [33], [34] is more sensitive than human fingertips and previous tactile lump detectors. However, these works only roughly estimate the lump map by directly showing the tactile images. In this article, we make a further step based on these works to estimate the 3-D elasticity distribution inside the target object from vision-based tactile signals.

C. Robot-Assisted Palpation

Most previous robot-assisted palpation methods are based on unidirectional pressing and sliding. Several earlier methods depend on pressing and generating a tactile map on the surface [1], [2], [35], [36]. Kim et al. [37] designed an exemplar circular probe for lump palpation using the contact pressure distribution in sliding. These methods only produce a 2-D distribution of properties on contact surfaces. Inspired by the actual finger motions in palpation, Ahn et al. [5] located abnormal tissue in the diagnosis of prostate cancers.

With the popularity of machine learning techniques, more methods based on neural networks have been applied in the palpation of abnormal inclusions. Xiao et al. [6] used a palpation probe equipped with a force sensor to capture force and displacement signals. It estimates the depth of the inclusion through deep recurrent neural networks. With the high dimensional tactile array assembled in the robot end-effector, Zhou et al. [38] solved the classification problem of tumor depth estimation based on the 2-D convolutional neural network with long short-term memory structures. However, these methods rely on well-collected training data and only classify the depth in a small set of quantified values. Users are not able to observe the morphology of the inclusions.

III. Method

A. Overview

Our goal of tactile elastography is to reconstruct the internal elasticity distribution of interactive soft materials through external observed contacts. We sample t steps of tactile signals during a single press, capturing both the nodal displacements $\mathbf{x}_s^{(i)} \in \mathbb{R}^{3n_s}$ and the global displacement of the sensor $\mathbf{d}^{(i)} \in \mathbb{R}^3$ at each step i, where n_s represents the number of nodes on the sensor. The data sequence $\{\mathbf{x}_s^{(i)}, \mathbf{d}^{(i)}\}_{i=1,2,\ldots,t}$ encode the time-varying tactile information for pressing excitation. With the sensor's initial configuration known as $\mathbf{x}_s^{(0)} \in \mathbb{R}^{3n_s}$, the deformation at each node v and step i is computed as $\mathbf{u}_s^{(i)}(v) = \mathbf{x}_s^{(i)}(v) - \mathbf{x}_s^{(0)}(v)$. The number of nodes in the object geometry is denoted as n. Assuming the initial geometry $\mathbf{x}^{(0)} \in \mathbb{R}^{3n}$ of the object is known from vision-based reconstructions [39], we aim to determine the distribution of the object's Young's modulus, which reflects material softness [40]. This modulus is discretized into elements $\mathbf{e} = \{e_1, \ldots, e_m\} \in \mathbb{R}^m$, where m is the number of elements and e_i represents the modulus of the ith element.

Given that vision-based tactile sensors feature soft layers sensitive to deformation, we hypothesize that these deformations serve as indicators of the object's internal elasticity. However, deriving the elasticity distribution from surface contact signals is complex due to dependencies on contact dynamics and material properties. Therefore, modeling the relationship between tactile data and the elasticity map is necessary. We employ the finite element method (FEM) to address the inverse problem of estimating material properties from observed deformations.

Our methodology involves a pipeline (see Fig. 2) that uses simulation tools to tackle the challenges of tactile elastography. We set node positions on the tactile sensor and the sensor's global displacements as inputs. Based on the static equilibrium of the sensor model, the external force $\mathbf{f}_s^{(i)} \in \mathbb{R}^{3n_s}$ on the sensor is obtained by FEM using the deformation field $\mathbf{u}_s^{(i)} \in \mathbb{R}^{3n_s}$ at each sampling step i. We calculate the external force $\mathbf{f}_o^{(i)} \in \mathbb{R}^{3n}$ using force equilibrium at the contact points. We then convert sensor deformations $\mathbf{u}_s^{(i)}$ to global coordinates to match with the object's deformations $\mathbf{u}_o^{(i)} \in \mathbb{R}^{3n_c}$, where n_c is the number of contact surface nodes. An initial guess of elasticity distribution $\mathbf{e}^* \in \mathbb{R}^m$ informs an optimization process to refine the estimate $\hat{\mathbf{e}} \in \mathbb{R}^m$, ensuring the simulated deformation $\hat{\mathbf{u}} \in \mathbb{R}^{3n}$ fits the observed deformation $\mathbf{u}_o$.

This work assumes quasistatic motion, no slip at the contact interface, and isotropic material properties, simplifying our analysis and ensuring stability in our tactile measurements. We summarize all the key variables in Nomenclature. Because both the sensor and the target object are involved in the computation, we use the subscripts s to indicate the corresponding physical quantities on the sensor. At the same time, as we actively sample many frames from each pressing trial, we use the superscript (i) to indicate the signal at the ith time step, while we keep using the same superscript at the 0th time step to denote the rest geometry.

B. Simulation Model

In a system of materials subjected to forced deformation, obtaining a closed-form solution for the equilibrium differential equations of a continuum hyperelastic body is challenging. Therefore, given the object's geometry, we use FEM to simulate its elastic energy and deformation during interaction. Since we also aim to optimize the material distribution using the

IEEE Transactions on Robotics (T-RO) paper, presented at ICRA 2026, Vienna, Austria. Cite as T-RO paper.

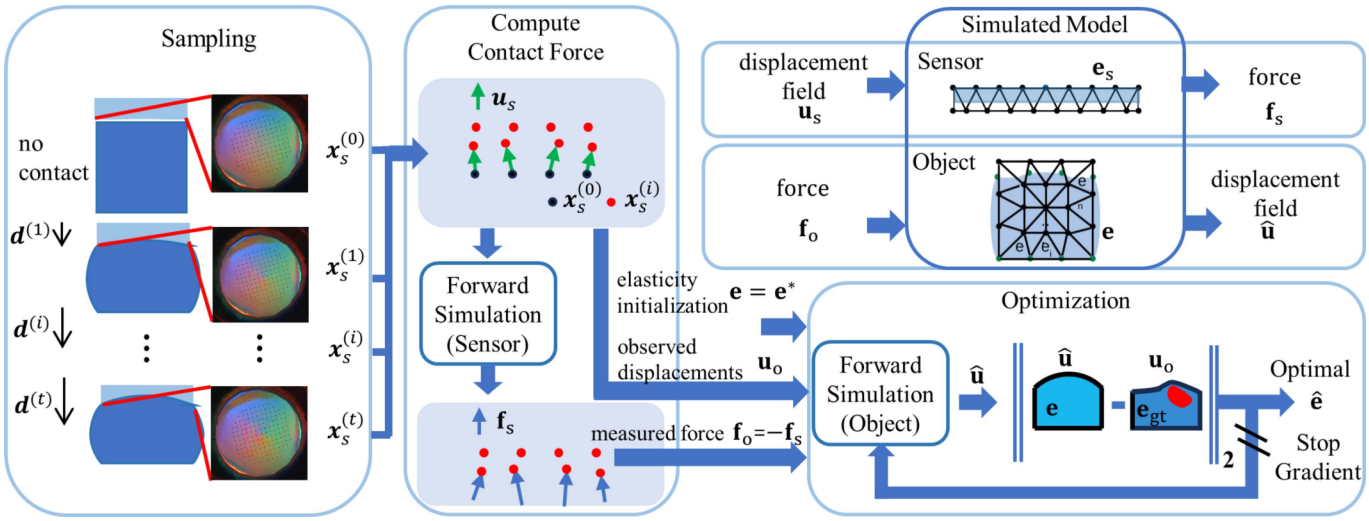

Fig. 2. Overall framework of tactile elastography. At the sampling step i, nodal positions $\mathbf{x}_s^{(i)}$, and displacements $\mathbf{u}_s^{(i)}$ on the tactile surface are obtained during the pressing process. Contact forces on the sensor $\mathbf{f}_s$ and the object $\mathbf{f}_o$ are computed through forward simulation. In the optimization block, a suitable elasticity distribution $\mathbf{e}$ is identified to minimize the difference between the predicted deformation $\hat{\mathbf{u}}$ under the external force $\mathbf{f}_o$ and the observed displacement $\mathbf{u}_o$ on the target object.

simulation model as the predictor, we couple a simple elasticity distribution representation with the FEM of the soft object.

Suppose the target object is meshed into n nodes and m elements (tetrahedra for 3-D cases). The nodal displacements are written as $\mathbf{u}$, and $\mathbf{f}_o$ represents the observable external nodal force. The energy in the whole system can be estimated as follows:

$$E(\mathbf{u};\mathbf{e},\mathbf{f}_o) = E_d(\mathbf{u};\mathbf{e}) + E_c(\mathbf{u}) + E_f(\mathbf{u},\mathbf{f}_o). \tag{1}$$

The overall energy of the quasistatic model consists of the elastic potential energy $E_d(\mathbf{u};\mathbf{e})$, the constraint energy $E_c(\mathbf{u})$, and the force potential $E_f(\mathbf{u},\mathbf{f}_o)$ in the loaded system.

1) Elastic Potential Energy: The elastic potential is produced by the deformation of elastic objects. In this work, we employ the Neo-Hookean material model, and the elastic potential energy density Ψ in an element is as follows:

$$\Psi(\mathbf{u};\mathbf{e}) = \frac{\mu}{2}\mathrm{tr}(\mathbf{F}^T\mathbf{F}-\mathbf{I}) - \mu\ln J + \frac{\lambda}{2}(\ln J)^2 \tag{2}$$

where $\mathbf{F}\in\mathbb{R}^{3\times3}$ is the deformation gradient, $\mathbf{I}\in\mathbb{R}^{3\times3}$ is an identity matrix, $J=\det(\mathbf{F})$ represents the Jacobian matrix, $\lambda = e\nu/(1+\nu)(1-2\nu)$, $\mu = e/2(1+\nu)$ are the Lame constraints, e is the value of Young's modulus, and ν is the Poisson's ratio. The total elastic potential energy is computed as the volume-weighted summation of the elastic potential density.

2) Constraint Energy: We formulate constraint energy by defining zero-length springs on the fixing nodes, which ensures the bottom of the object to be tested is fixed in the simulated environment. We have

$$E_c(\mathbf{u}) = \frac{1}{2}||\mathbf{A}\mathbf{u}||_2 \tag{3}$$

where $\mathbf{A}\in\mathbb{R}^{3n\times3n}$ is defined as $\mathbf{A}=k_c\mathbf{C}$, $\mathbf{C}\in\mathbb{R}^{3n\times3n}$ is the selection matrix for the constraint nodes, and k_c is the stiffness of the constraint zero-length spring.

3) Force Potential Energy: The force potential E_f is gained by loaded force, namely, the gravitational potential energy $E_g(\mathbf{u})$ and the external force potential $E_o(\mathbf{u},\mathbf{f}_o)$ in our settings. We have

$$E_f(\mathbf{u};\mathbf{f}_o) = E_g(\mathbf{u}) + E_o(\mathbf{u},\mathbf{f}_o) = \mathbf{m}^T g\mathbf{h} - \mathbf{f}_o\mathbf{u} \tag{4}$$

where $\mathbf{m}\in\mathbb{R}^n$ is the mass vector associated with the nodes, g is the gravitational constant, and $\mathbf{h}\in\mathbb{R}^n$ is the vector containing the heights of nodes, which are determined by the displacement of each node.

In forward simulation for the object, an optimization formulation is introduced to find the solution of $\mathbf{u}$ in the quasistatic system

$$\hat{\mathbf{u}} = \underset{\mathbf{u}}{\mathrm{argmin}}\, E(\mathbf{u};\mathbf{e},\mathbf{f}_o). \tag{5}$$

The optimized deformation $\hat{\mathbf{u}}\in\mathbb{R}^{3n}$ with the minimal energy in the overall system meets the first-order condition mentioned as force equilibrium as follows:

$$\begin{aligned}\mathbf{f}(\mathbf{u};\mathbf{e},\mathbf{f}_o) &= -\partial E(\mathbf{u};\mathbf{e},\mathbf{f}_o)/\partial\mathbf{u} \\ &= \int_0^{\mathbf{u}} K(\mathbf{u};\mathbf{e})d\mathbf{u} - \mathbf{A}(\mathbf{u}-\mathbf{u}') - (\mathbf{m}^T g - \mathbf{f}_o) = \mathbf{0}\end{aligned} \tag{6}$$

where $\mathbf{K}(\mathbf{u};\mathbf{e}) = -\frac{\partial^2\phi}{\partial\mathbf{u}^2}\in\mathbb{R}^{3n\times3n}$ is the global stiffness matrix for the object. In order to solve the deformation $\mathbf{u}$ given the external force $\mathbf{f}_o$ from the above equation, numerical methods are commonly used and we choose the Newton–Raphson method in our implementation.

At the other end, we compute the force $\mathbf{f}_s$ exerted on the sensor by implementing the forward simulation for the sensor. Given the measured deformation $\mathbf{u}_s$ and the known material parameters $\mathbf{e}_s$ of the soft layer, the nodal force $\mathbf{f}_s$ is the solution of the linear equation $\mathbf{f}(\mathbf{u}_s;\mathbf{e}_s,\mathbf{f}_s)=0$.

C. Inverse Problem

In the preceding section, we formulate a quasistatic forward model to compute the corresponding nodal displacement $\hat{\mathbf{u}}$ to an elasticity distribution $\mathbf{e}$ among elements with an observed nodal forces $\mathbf{f}_o$. Here, by perceiving the nodal displacement $\mathbf{u}_o$ on the contact surface, we propose an inverse formulation of the forward model aimed at reconstructing elasticity distribution $\mathbf{e}$ of the object. We encode the goal that the simulated displacements $\mathbf{u}$ match the observed deformation field $\mathbf{u}_o$ into the reduced form of shape objective

$$\hat{O}_{\text{shape}}(\mathbf{e}) = O_{\text{shape}}(\mathbf{u}(\hat{\mathbf{e}})) = \frac{1}{2}\sum_{i=1}^{t} ||\mathbf{S}^{(i)}\hat{\mathbf{u}}^{(i)}(\mathbf{e}) - \mathbf{u}_o^{(i)}||_2^2 \quad (7)$$

where $\mathbf{S}^{(i)} \in \mathbb{R}^{3n_c \times 3n}$, and $\hat{\mathbf{u}}^{(i)}$ are the selection matrix, the current nodal displacement in the ith sample, respectively. Given an initial value $\mathbf{e}^*$, we seek the optimal $\hat{\mathbf{e}}$ by a truncated-Newton method (TNC) to minimize the $\hat{O}_{\text{shape}}$ as follows:

$$\hat{\mathbf{e}} = \underset{\mathbf{e}}{\text{argmin}}\, \hat{O}_{\text{shape}}(\mathbf{e}) \quad (8)$$

which approximates the deformation of the object to the observations. The corresponding gradient $\frac{d\hat{O}_{\text{shape}}}{d\mathbf{e}}$ is necessary for performing the optimization in (8). Applying the chain rule, we have the following:

$$\frac{d\hat{O}_{\text{shape}}}{d\mathbf{e}} = \sum_{i=1}^{t} \frac{\partial O_{\text{shape}}}{\partial \hat{\mathbf{u}}^{(i)}} \frac{d\hat{\mathbf{u}}^{(i)}}{d\mathbf{e}}. \quad (9)$$

Based on the static equilibrium discussed in Section III-B, we have $\mathbf{f}(\mathbf{u}(\hat{e}); \mathbf{e}, \mathbf{f}_o) = 0$. Because the external forces $\mathbf{f}_o$ on the object is known, we yield a total derivative of the resultant force

$$\frac{d\mathbf{f}}{d\mathbf{e}} = \frac{\partial \mathbf{f}}{\partial \mathbf{e}} + \frac{\partial \mathbf{f}}{\partial \hat{\mathbf{u}}}\frac{d\hat{\mathbf{u}}}{d\mathbf{e}} = \mathbf{0}. \quad (10)$$

It contributes to the computing of $\frac{d\hat{\mathbf{u}}}{d\mathbf{e}} = -(\frac{\partial \mathbf{f}}{\partial \hat{\mathbf{u}}})^{-1}\frac{\partial \mathbf{f}}{\partial \mathbf{e}}$, where both of the partial derivatives are easily accessible. Since the expression of $\mathbf{f}$ is given in (6), we have $\frac{\partial \mathbf{f}}{\partial \hat{\mathbf{u}}} = K(\hat{\mathbf{u}}; \mathbf{e}) - \mathbf{A}$. For the partial derivative of $\mathbf{f}$ with respect to the element elasticity $\mathbf{e}$, we have

$$\frac{\partial \mathbf{f}}{\partial \mathbf{e}} = [\mathbf{f}_{\text{int}}(\hat{\mathbf{u}}, \mathbf{a}_1), \ldots, \mathbf{f}_{\text{int}}(\hat{\mathbf{u}}, \mathbf{a}_j), \ldots] \quad (11)$$

where the internal nodal elastic force $\mathbf{f}_{\text{int}}(\hat{\mathbf{u}}, \mathbf{e})$ can be obtained as the gradient of the elastic potential $\frac{\partial \phi}{\partial \hat{\mathbf{u}}}$, $\mathbf{a}_1 = [1, 0, .., 0], \ldots, \mathbf{a}_j = [0, ..1, \ldots, 0], j = 1, \ldots, m$ is a set of orthogonal basis vectors. Hence, the gradient is formulated as follows using the chain rule:

$$\frac{d\hat{O}_{\text{shape}}}{d\mathbf{e}} = -\sum_{i=1}^{t}(\mathbf{S}^{(i)}\hat{\mathbf{u}}^{(i)} - \mathbf{u}_o^{(i)})\frac{d\hat{\mathbf{u}}}{d\mathbf{e}}|_{\hat{\mathbf{u}}=\hat{\mathbf{u}}^{(i)}} \quad (12)$$

$$\frac{d\hat{\mathbf{u}}}{d\mathbf{e}}|_{\hat{\mathbf{u}}=\hat{\mathbf{u}}^{(i)}} = -(\mathbf{K}(\hat{\mathbf{u}}^{(i)}; \mathbf{e}) - \mathbf{A}^{(i)})^{-1}\frac{\partial \mathbf{f}}{\partial \mathbf{e}}|_{\hat{\mathbf{u}}=\hat{\mathbf{u}}^{(i)}} \quad (13)$$

where $\mathbf{K}(\hat{\mathbf{u}}^{(i)}; \mathbf{e})$ and $\mathbf{A}^{(i)}$ are the global stiffness matrix and the constraint matrix at the ith time step, respectively. The inverse solver is shown in Algorithm 1. To ensure that forward simulation will not cause excessive distortion, we set upper bound e_u and lower bound e_l for Young's modulus in optimization.

Algorithm 1: Inverse Solver.

DATA External force $\mathbf{f}_o$, target nodal displacement $\mathbf{u}_o$, initial elastic distribution $\mathbf{e}^*$
RESULT Elasticity distribution $\mathbf{e}$
$\mathbf{e} \leftarrow \mathbf{e}^*$
$i \leftarrow 0, d\hat{O}_{shape}/d\mathbf{e} \leftarrow \infty$
While $d\hat{O}_{shape}/d\mathbf{e} > \epsilon$
  While i<p
    $\hat{\mathbf{u}}^{(i)} \leftarrow ForwardSimulator(\mathbf{e}, \mathbf{f}_o^{(i)})$
    $\hat{O}_{shape,i} = \frac{1}{2}||\mathbf{S}^{(i)}\hat{\mathbf{u}}^{(i)} - \mathbf{u}_o^{(i)}||_2$
    $d\hat{O}_{shape,i}/d\mathbf{e} \leftarrow GradientSolver(\hat{O}_{shape}^{(i)}, \mathbf{e})$
    $i \leftarrow i + 1$
  $d\hat{O}_{shape}/d\mathbf{e} \leftarrow Sum(d\hat{O}_{shape}^{(i)}/d\mathbf{e})$
  $\mathbf{e} \leftarrow \mathbf{e} + TNC(d\hat{O}_{shape}/d\mathbf{e})$

D. Sensitivity Analysis

In this section, our primary focus lies on investigating whether the interior stiffness distribution is reliably estimated simply from the surface observable. We leverage a derivative-based local approach for sensitivity analysis, aiming at assessing how material perturbations affect the surface deformation observed by the tactile sensor. From our previous physics-based model, we derive the Jacobian matrix of nodal displacement concerning Young's modulus, denoted as $\frac{d\hat{\mathbf{u}}}{d\mathbf{e}}$ in (13). This $n \times m$ matrix's (i, j)th element represents the change in displacement of the ith node due to infinitesimal perturbation in the stiffness of the jth element within the object. We further apply a selection matrix $\mathbf{S}$ to focus on the observable deformation of the surface nodes, yielding

$$\mathbf{M}_{n_c \times m} = \mathbf{S}_{n_c \times n}\frac{d\hat{\mathbf{u}}}{d\mathbf{e}}_{n \times m}. \quad (14)$$

Thus, with the matrix $\mathbf{M} = [m_{i,j}] \in \mathbb{R}^{n_c \times m}$, the sensitivity of the ith surface node to the stiffness update of the jth element is given by $m_{i,j}$.

1) Credibility Metric: To facilitate the visualization of sensitivity, we define a relative credibility metric.

$$L(j) = \max_i |m_{i,j}|, i = 1, \ldots, n_s, j = 1, \ldots, m \quad (15)$$

which indicates the maximum influence of the stiffness of the jth element on the surface deformation. If the credibility metric for a specific element is low, the error in its estimated stiffness will cause only a tiny difference in the surface deformation, which may not be detected by the tactile sensor, resulting in an unreliable stiffness estimation for that element. Consequently, we expect the stiffness estimation to be more reliable at positions where the credibility metric is high.

2) Influence Factors of Credibility: We use a representative model to visualize the credibility metric intuitively. In Fig. 3, we select a unit cube model with homogeneous material, with

IEEE Transactions on Robotics (T-RO) paper, presented at ICRA 2026, Vienna, Austria. Cite as T-RO paper.

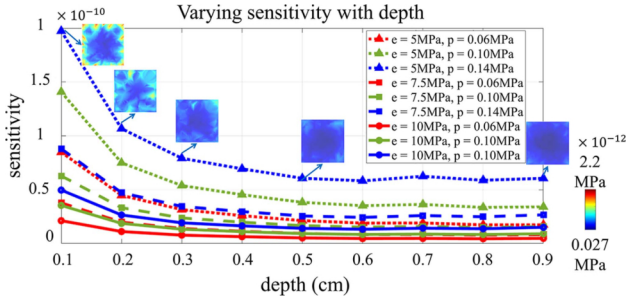

Fig. 3. Sensitivity of elastography results with respect to depth. The integrated credibility metric is plotted along slices of the z-axis under varying external pressure for objects with different stiffness levels. The observed tactile signals exhibit greater sensitivity to the material properties at shallower layers.

Young's modulus values of 5 MPa, 7.5 MPa, and 10 MPa. Different pressures (0.06 MPa, 0.10 MPa, and 0.14 MPa) are applied to the top of the model to investigate the distribution of the credibility metric for the estimated stiffness from tactile elastography. Since the credibility metric forms a scalar field within the target object, we plot slices of heat maps at various layers to visualize the credibility, as shown in the subplots of Fig. 3. The figure indicates that elements in the shallow layers exhibit greater reliability. Within the same layer, surface deformation is more sensitive to elements near the boundary, while the elasticity of deeper elements contributes less to the surface deformation.

We further examine the differences in credibility levels when objects with varying stiffness are subjected to different pressure levels. We integrate the credibility metric across different layers to visualize the trend, as shown in the line plots in Fig. 3. The results indicate that the estimated elasticity values at shallow layers are consistently more reliable than those at deeper layers. This finding suggests that properties at greater depths are more difficult to perceive, whereas shallower layers provide more reliable perceptual information. Comparing the curves under different external pressures in Fig. 3 reveals that higher pressures extend the range of accurate perception to greater depths. In addition, variations in elasticity reveal that softer materials exhibit higher sensitivity, indicating a larger perception range in soft objects compared to harder ones. Both increased external pressure and softer materials enhance depth perception, which is consistent with our real-life experiences. These observations allow us to provide a credibility measurement for the tactile elastography results. They also offer insights into the choice of design factors in tactile elastography, which will be further explored and discussed in Section IV-B.

IV. Experiment Results

A. Results

In this section, we evaluated our method of tactile elastography in simulated environments with the known ground-truth distribution of the material by applying pressures on sampling points (see details of sampling strategy in Section V-C).

1) Setup: In the following experiments, we set the hyperparameter $k_c = 1000$ to ensure rigid attachment of the nodes at the bottom of the models. In addition, Young's modulus of elements was constrained in the range $[e_l, e_u]$, where $e_l = 0.001$ MPa and $e_u = 100$ MPa. For the experiment, the initial Young's modulus is set to a uniform distribution of 0.2 MPa. The mesh was divided into tetrahedrons with their average edge length set to at most 10% of the diagonal length of its bounding box. We implemented and evaluated our method on a desktop running ubuntu18.04 with an Intel $i7-11700U$ CPU 3.60 GHz. In our study, we used scipy.optimize package in Python to solve the minimization problem.

2) Metrics: To assess the relative difference of the elasticity distributions $\mathbf{e}$, we compute the structural similarity SSIM($\hat{\mathbf{e}}, \mathbf{e}_{\text{gt}}$) [41], the normalized correlation as the metric $s(\hat{\mathbf{e}}, \mathbf{e}_{\text{gt}}) = \frac{|(\mathbf{e}_{\text{gt}} - \bar{\mathbf{e}}_{\text{gt}})(\hat{\mathbf{e}} - \bar{\hat{\mathbf{e}}})|}{|(\mathbf{e}_{\text{gt}} - \bar{\mathbf{e}}_{\text{gt}})||(\hat{\mathbf{e}} - \bar{\hat{\mathbf{e}}})|}$, the peak signal-to-noise ratio PSNR($\hat{\mathbf{e}}, \mathbf{e}_{\text{gt}}$) [42], and we also report the root mean square error RMSE($\hat{\mathbf{e}}, \mathbf{e}_{\text{gt}}$) [43] where $\mathbf{e}_{\text{gt}}$ is the ground truth of the elasticity distribution. Normalized correlation is commonly used to assess the integrated similarity of the signals [8]. These metrics are representative assessment metrics in medical imaging quality assessment tasks [44], which are proven to have strong positive correlations with subjective assessment scores. The higher SSIM, normalized correlation s and PSNR, and the lower value of RMSE indicate higher accuracy.

3) Test Models: We constructed diverse models to test our approach, including two-material models and heterogeneous models of different geometries. For tests of two-material cases, we built cubic models, as well as cylindrical, hyperbolical, and hemispherical models, which represent typical second-order curved geometries, with inclusions of various shapes in Fig. 4. Note that we presented the test for distributed inclusion in Fig. 4(g). In Fig. 4(d), we design a cubic model embedded with a soft cone-shaped inclusion. Then, we experimented on three heterogeneous models, including heterogeneous cube and hemisphere models in Fig. 5. All the ground truths of the test models are displayed in the upper row of Figs. 4 and 5.

4) Test Results: The accuracy metrics and elastography results compared to corresponding ground truths are illustrated in Figs. 4 and 5. We found a strong correlation between the ground-truth map and the tactile elastography from the results shown in the figures. The statistics listed in Figs. 4 and 5 in terms of the SSIM, normalized correlation, PSNR, and RMSE, demonstrate similar levels of indicators in [45], [46]. Therefore, it can be seen that our method provided recovery and showed its agreement with the input map as well for objects' elasticity with two material distributions or heterogeneous distributions.

We then compared the computational cost of tactile elastography with existing medical imaging methods. Basic 2-D imaging using X-ray for a voxel size of 0.4 mm takes less than 15 min on central processing units (CPU: 2.13 GHz, RAM: 32 GB) [47], and the average computation time for converting 2-D to 3-D is around 3 min [48]. The calculation in USE for volume data within a 60 mm depth can be performed in parallel over a few seconds [49]. The computation time for 3-D MRE varies, ranging from a few seconds to several hours, depending on the quality requirements and the chosen method [50]. Notably, achieving real-time computation in milliseconds, as with 2-D ultrasound imaging, remains a challenge for current 3-D elastography techniques. The computation time of our optimization

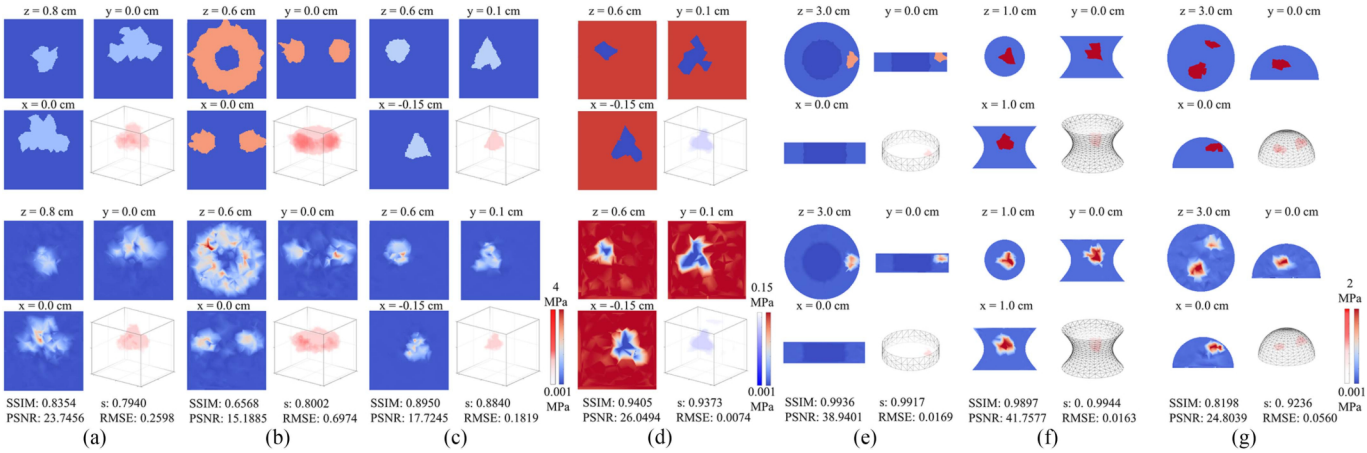

Fig. 4. Elastography results for models with two material types. The upper row illustrates the ground truths, and the lower row displays the corresponding elastography results. (a) Cube with a hard two-tier cake-shaped inclusion. (b) Cube with a hard torus. (c) Cube with a hard cone. (d) Cube with a softer cone. (e) Cylinder with a hole and an inclusion. (f) Hyperboloid with an inclusion. (g) Hemisphere with distributed inclusions.

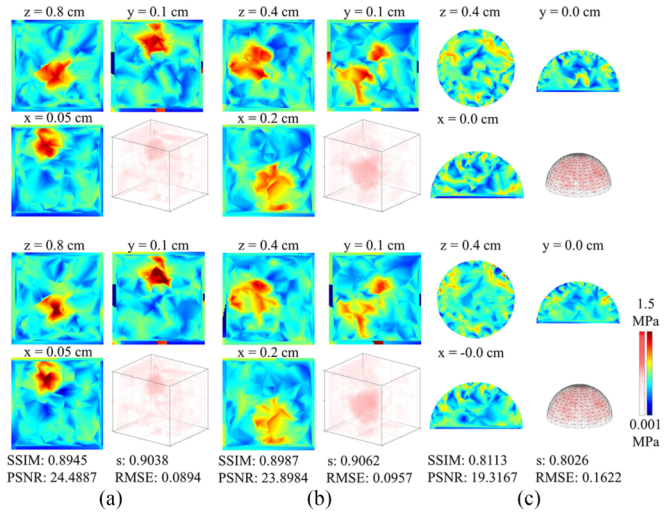

Fig. 5. Elastography results for three models with heterogeneous materials. The upper row shows the ground truth material distributions, and the lower row presents the corresponding elastography results. (a) and (b) Heterogeneous cubes. (c) Heterogeneous hemisphere.

TABLE I
COMPUTATION COST

Models	#Ele	Sec/Iter	SSIM		
			100 Iters	500 Iters	2500 Iters
Fig. 4(a)	2485	1.53	0.3597	0.6950	0.8019
Fig. 4(b)	3130	1.98	0.0463	0.2106	0.5856
Fig. 4(c)	1519	0.36	0.4714	0.7846	0.8651
Fig. 4(d)	1130	0.34	0.7336	0.7787	0.8205
Fig. 4(e)	1739	0.29	0.2720	0.3698	0.6171
Fig. 4(f)	2164	1.20	0.6819	0.9364	0.9974
Fig. 4(g)	1935	0.67	0.4799	0.6337	0.7990
Fig. 5(a)	1130	0.34	0.5676	0.7451	0.8418
Fig. 5(b)	1130	0.34	0.5991	0.8353	0.8745
Fig. 5(c)	1935	0.65	0.4799	0.6796	0.7191

problem primarily depended on the complexity of the geometry model and the material distribution. Here, we demonstrated the computation cost table in Table I for geometry models in Figs. 4 and 5. We found that tactile elastography took less than 6 min for models with about a thousand of nodes to produce a meaningful distribution without hardware acceleration. Similar to previous 3-D medical imaging methods, our approach achieved an acceptable computational cost for elastography. However, its feasibility for real-time applications remains limited by the higher computational complexity of the inverse FEM. Given the tradeoff between speed and resolution, tactile elastography is well-suited for tasks involving precomputation or low update frequency. Its accessibility and simplicity make it ideal for preliminary clinical diagnoses, such as detecting lesion tissue, enabling easy self-examinations, and facilitating remote palpation. Furthermore, as discussed in Section VII, it holds potential for acceleration in real-time applications.

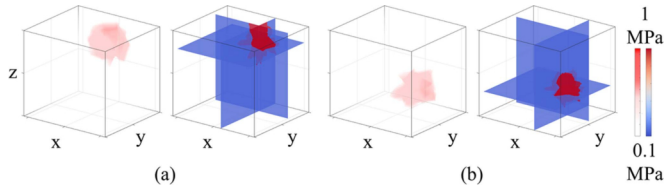

Fig. 6. Cubic models with inclusions at different depths for studying design factors. (a) Model 1: Inclusion at a shallow layer. (b) Model 2: Inclusion at a deep layer.

B. Design Factors

In this section, we experimented with different design factors in tactile elastography to justify their influence on the quality of the results. In this experiment, we chose two unit cubes with two spherical hard inclusions in different depths as shown in Figs. 6 and 7(a). Then, we tested our method with different experimental settings to indicate how deep the press should be, how many sampled frames we need, and whether pressing along multiple directions was significant in tactile elastography with the experimental results shown in Fig. 7. We also adjusted the range of the color map to better visualize the scalar map for different comparisons.

IEEE Transactions on Robotics (T-RO) paper, presented at ICRA 2026, Vienna, Austria. Cite as T-RO paper.

TABLE II
ACCURACY METRICS FOR DIFFERENT SITUATIONS

Model	Metrics	$p_{\max}$ (MPa)				t				dir			SNR(dB)	
		0.09	0.12	0.15	0.18	2	3	5	9	1	2	3	20	10
1	s ↑	0.6091	0.6625	0.7889	0.8144	0.7548	0.7952	0.7972	0.8037	0.8211	0.8477	0.8839	0.8810	0.5377
	SSIM ↑	0.3271	0.4104	0.6852	0.7467	0.6150	0.7044	0.7075	0.7334	0.7614	0.7858	0.8348	0.8545	0.4520
	PSNR ↑	18.441	18.948	21.066	21.693	20.438	21.266	21.302	21.467	21.854	22.449	23.519	23.103	12.377
	RMSE (MPa) ↓	0.1195	0.1128	0.0884	0.0822	0.0950	0.0864	0.0860	0.0844	0.0807	0.0754	0.0667	0.0699	0.2403
2	s ↑	0.2221	0.3435	0.3523	0.3654	0.3365	0.3479	0.3609	0.3507	0.3749	0.7357	0.8191	0.8396	0.4711
	SSIM ↑	0.1415	0.1918	0.1948	0.0.2303	0.2042	0.2094	0.2405	0.2552	0.2526	0.6853	0.7762	0.8382	0.4094
	PSNR ↑	17.943	18.217	18.235	18.316	18.223	18.254	18.316	18.295	18.363	21.021	22.370	22.615	12.053
	RMSE (MPa) ↓	0.1266	0.1227	0.1224	0.1213	0.1226	0.1221	0.1213	0.1216	0.1206	0.0888	0.0760	0.0739	0.2494

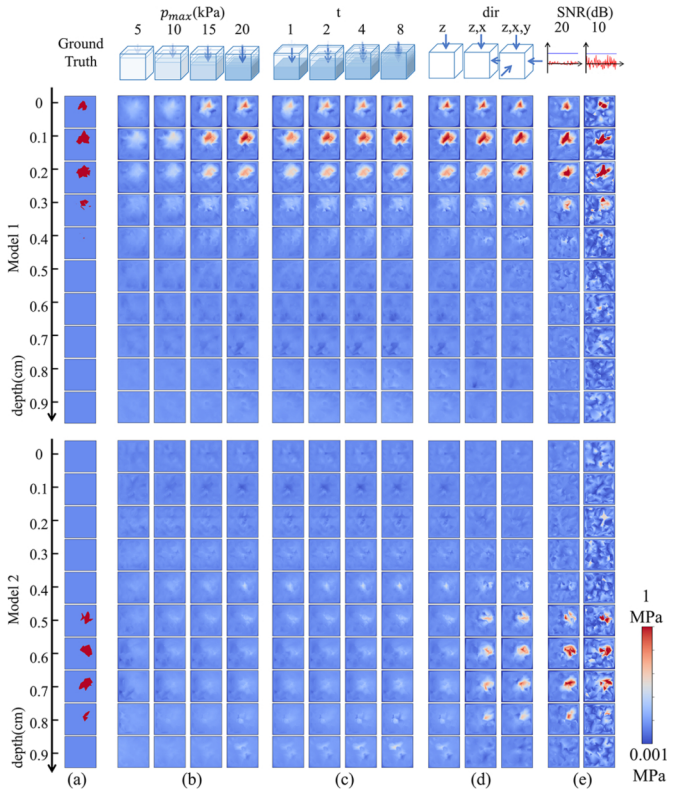

Fig. 7. Elastography results for the simulated models shown. The upper row illustrates the images for Model 1, and the lower row illustrates the images for Model 2. (a) Ground truth. (b) Results for varying external pressure ranges. (c) Results for different sampling resolutions. (d) Results for varying the number of sampling directions. (e) Results with noisy inputs.

1) Range of External Pressure: First, we experimented to find how the quality of tactile elastography varies with respect to the magnitude of each pressing test. As a deep press of an object could be quantified as the overall magnitude of the pressing force, we would take the range of external pressure as the design factor in this experiment. As analyzed in Section III-D, the features deep inside the object were less sensitive to tactile elastography. We expected the larger external pressure would better reveal the material distribution in the deep regions. Therefore, We tested the tactile elastography with four levels of the maximum pressure $p_{\max}$ ranging from 5 kPa to 20 kPa with a step size $r = 5$ kPa, exerted from one direction on the object. The experimental results were summarized in Fig. 7(b). We also evaluated the similarity scores of the recovered elastography to the ground truth and listed them in Table II.

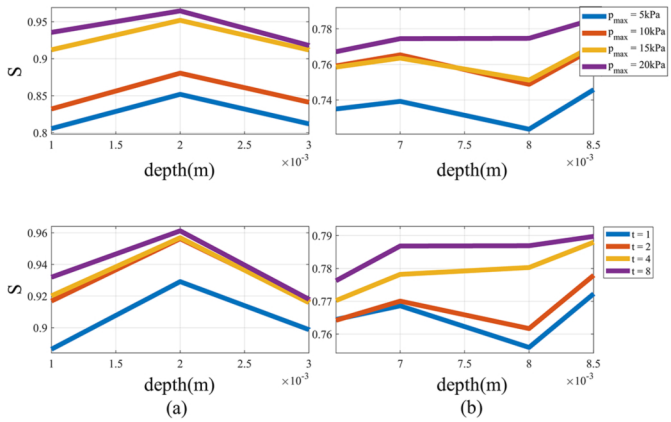

Fig. 8. Similarity of elastography results at varying depths where the hard inclusions are located under different conditions. The upper row shows trends for varying maximum external pressures, while the lower row illustrates trends for different external pressure resolutions. (a) Trends correspond to Model 1. (b) Trends correspond to Model 2.

As displayed in Fig. 7(b), we observed that applying larger external pressures could bring a more sensitive perception of deeper layers in objects. To further investigate the reconstruction capability influenced by the range of external pressures from the shallow area to the deep region in the specific model, we computed the credibility value for each layer to its ground truth from the top to the bottom and plotted in the upper row of Fig. 8. We found increasing sampling times by utilizing a larger range of external pressure with a constant resolution brings a deeper perception along the sampling direction, which is according to our perspective in Section III-D. However, simply increasing the range of p does not have a significant effect on tactile elastography except for expanding perceiving depth.

On the one hand, with the same number of sampling frames, a high $p_{\max}$ would lead to a large sampling gap between the frames and the details of the distribution would be lost with a low sampling resolution in the pressing. On the other hand, because we could not apply an extremely large pressure on the object for safety, the pressure that we actively exerted in the experiment still had an upper bound, which also limited the perception depth along a certain direction.

2) Sampling Resolution: Now, we experimented with our method with different sampling resolutions. As the spatial resolution was determined by the vision-based tactile sensor, here we referred to the sampling resolution as the number of temporal samples during the pressing process. We would check how the quality of the proposed tactile elastography would update

with more sampling frames sent to the computational pipeline. Therefore, we kept the same pressure range with its upper bound 20 kPa, and the pressing direction was set along the z-axis. As for the control variable, we took the sampling times $t \in \{1, 2, 4, 8\}$. We provided the tactile elastography in Fig. 7(c) and accompanied the statistics in Table II as well.

From the experimental results, an increasing trend of the quality was found with the higher sampling resolution. Higher sampling resolution brings more observable data in a certain perceiving depth owing to the range limitation of the force. As a result, we found in the layers of elasticity maps that with the increase of the sampling resolution, a finer perception was obtained under a certain depth. The elastography was better improved at shallow layers when the sampling resolution increased and the improvement was not that observable for deep layers. This matched with our discussion in the last experiment, as the upper bound of the external force was limited and its influence was nonnegligible. Then, we inspected the similarity scores for each layer to its ground truth from the top to the bottom and plotted them in the lower row of Fig. 8. Although the improvements of the whole distribution are limited, we found a notable increase of the similarity score in the abnormal area with a higher resolution of pressure in a certain range applied in the test.

3) Pressing Directions: As discussed above, shallower layers in pressing directions were perceived better, and deeper layers were hard to reconstruct clearly due to the upper bound of forces. We, therefore, assumed that more pressing directions from different sides would help improve the perceptual capability of material distribution deep inside the object. In our experimental design, we adhered to a consistent resolution for presses while gradually augmenting the number of pressing directions.

We present the elastography results with additional pressing trials along more directions from the sides, as shown in Fig. 7(d). Through the examination of both the elastography results and the similarity metrics, more pressing directions contributed to improving the quality of the results. As the deep regions with respect to one pressing direction would be better observable in another direction, more information with high credibility in space was obtained with more pressing directions.

C. Noisy Inputs

So far, we assumed the input tactile signals and geometry of the target object were precisely measured for the experiments. In this section, we would test tactile elastography under varying levels of noise in the tactile images and the shape measurements.

1) Noisy Tactile Signals: To assess the impact of noisy tactile measurements, we introduced Gaussian noise into the tactile signals before we sent them for tactile elastography. We applied noises of two different levels to the sampling processes. The signal-to-noise ratios (SNR) were set to 20 dB and 10 dB, respectively, which were sufficiently high to cover the signal errors for typical vision-based tactile sensors [51]. The experimental results on the two tested objects were presented in Fig. 7(e).

As the observation noise of the tactile signals increased, the quality of the estimated elasticity distribution decreased. Despite this, the abnormal area corresponding to the inclusion could be recognized as well. As we proposed to use physics to extract the elastography, the dominant interior properties in objects could be recovered as long as the main characteristics in the map between the deformation and external force remained perceivable.

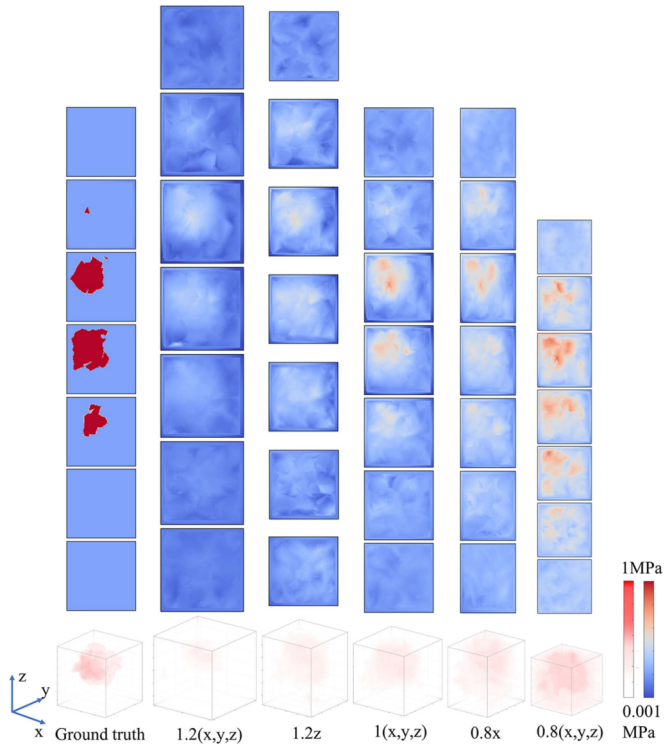

Fig. 9. Elasticity distribution results with shape estimation errors. The geometric models are resized from 80% to 120% along different axes.

2) Imperfect Geometric Measurements: Here, we experimented with our method using input models with imprecise geometric measurement. Typically, we asked for a well-captured rest shape of the target object for estimating the deformation field. Although the shape could be obtained using visual or tactile solutions, the reconstruction errors always existed and, therefore, may affect the quality of elastography. We tested our method to check the elastography when the shapes of the objects were measured to be larger or smaller due to the imperfect shape reconstruction. The rest shapes of the cubes were artificially enlarged or shrunk to 120% or 80% in an isotropic or anisotropic way, similar to [8]. We took these mismatched shapes for estimating the deformation with system errors and then produced the tactile elastography, as shown in Fig. 9.

From the results, we found that the interior distribution of elasticity was similar to the ground truth up to a certain scale. Under the same pressing operation, achieving the same nodal positions on a deformed surface required greater compression for materials with larger thickness in the pressing direction, resulting in a reduction of the stiffness in perception. Consequently, if the geometry model of the object was enlarged, the overall elasticity appeared softer. Conversely, if the geometry model was shrunk, the overall elasticity appeared stiffer as demonstrated in Fig. 9. We might still observe the suspicious region, which corresponded to the inclusion inside the object,

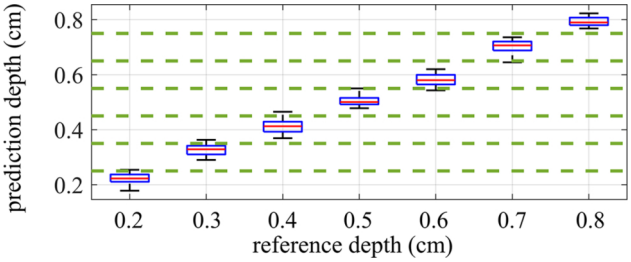

Fig. 10. Box plots of depth estimation results.

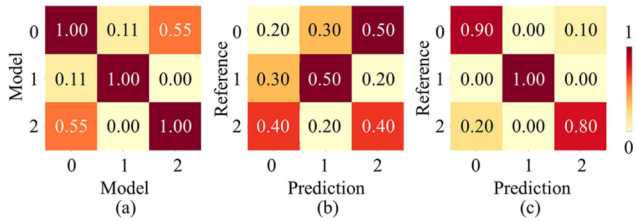

Fig. 11. Matrices from the inclusion recognition experiment. (a) Similarity matrix between the test models. (b) Confusion matrix from the human-based recognition experiment. (c) Confusion matrix from the elastography-based recognition experiment.

while its shape was also stretched due to the imprecise shape measurement of the tested object. Therefore, as long as the errors in the geometric measurements were predictable, users could read the elastography to estimate its interior material distribution.

V. Applications and Extensions

A. Depth Estimation

From the above results, we qualitatively and quantitatively evaluated the results of tactile elastography. Other than visually providing the interior stiffness information, we showed two applications to demonstrate the benefits of the rich information provided by tactile elastography. Specifically, we have checked the advantages of tactile elastography as the features for locating or recognizing hard inclusions inside soft materials.

Locating hard inclusions inside soft tissue from haptic cues has been studied in the literature, where the key challenge is to estimate the depth of the hard inclusions [52]. We hypothesize that the tactile elastography extracted using physics-based models will give abundant spatial information for this depth estimation task. Specifically, in this study, we embedded a spherical inclusion (stiffness: 30 MPa, radius: 2 mm) inside a soft cube model (stiffness: 4 MPa, side length: 1 cm) with random positions. Seven models of different depth levels were experimented in this study, where the depth of the inclusion was set as $d = 2, 3, \ldots, 8$ mm. We randomly positioned the inclusion inside the tissue to generate the samples at each depth. We used tactile elastography to generate the stiffness map, took the centroid for inclusion after thresholding the stiffness, and quantified its z-coordinate to classify its depth into seven groups. The estimated depths for the random samples were plotted in Fig. 10 using box plots. It visualized the consistency of depth estimation across different layers, highlighting both the central tendency. The average accuracy for the depth estimation of hard inclusions was 95% using our method. Compared to the learning-based method with the average accuracy 95.8% for four classes (0, 5, 8, 10 mm) in [6], our method achieved comparable accuracy for classifying seven groups of depth levels ($d = 2, 3, \ldots, 8$ mm). Note that generally, it is challenging to maintain accuracy when there are more groups in the classification problem. Moreover, the learning-based method relies on many reliable training samples while our method does not require collecting the samples with well-labeled depth. We also note that our method is capable of continuously estimating the location of the inclusion (the average error of the depth estimation was around 2.14%), while conventional classification solutions just classify the depth into a small number of groups.

B. Recognition

In palpation works, inclusion recognition is a difficult task due to the complexity of the shape of inclusions. The minor differences in the haptic cues are hard to perceive. We will show that tactile elastography could be applied to this task. By taking the tactile signals, the reconstructed stiffness map will work as a good feature for inclusion recognition. For this study, we experimented with three objects with different shapes of hard inclusions as mentioned in Fig. 4(a), (b), and (c). The reconstructed elasticity maps shown in the lower row of the Fig. 4(a), (b), and (c) and (e), (f), and (g) were visually distinguishable and showed the potential of tactile elastography in inclusion recognition. We further inspected the similarity metrics between the ground truth map of these objects. By comparing the SSIM of the 3-D scalar fields listed in Fig. 11(a), we found it is already very hard to distinguish the ground truth of stiffness maps. For example, the SSIM between the ground truth maps in Fig. 4(a) and (c) reached 0.55. We examined the inclusion recognition task with manual palpation tests. We fabricated the above three objects (detailed in Section VI-A) and then invited ten volunteers to press them and classify the shapes of their inclusions into a two-tier cake [see Fig. 4(a)], a torus [see Fig. 4(b)], or a cone [see Fig. 4(c)]. We drew the confusion matrix from human recognition in Fig. 11(b). The correctness ratio of the manual classification was around 36.7%, which was close to random selection. While it was difficult to manually recognize the shapes of inclusions only from tactile interaction, tactile elastography showed the advantages of machine intelligence to identify the subtle differences of the tactile signals. For comparison, we trained a fully convolutional network (FCN) [53], with 64 channels in the hidden layer. The input was Young's modulus distribution (e), to recognize elastography results. The model was trained using cross-entropy loss and optimized with the Adam optimizer. In total, we collected 150 elasticity distribution signals, corresponding to different inclusion shapes. We selected 120 signals as the training set, reserving the remaining 30 sets for testing. In Fig. 11(c), we present the confusion matrix for the elastography results corresponding to three different inclusion shapes [shown in Fig. 4(a), (b), and (c)]. The classification accuracy of the elastography results was 90%, which outperformed the manual recognition performance.

C. Sampling Strategy

In tactile elastography tasks involving novel objects, automatically determining optimal sampling points on the surface to comprehensively reconstruct the interior distribution is challenging. Therefore, a systematic sampling strategy is crucial for improving efficiency and generalizability in such applications. To address this, we employ a Bayesian-based approach [54] for selecting sampling points on the tactile surface. The goal is to iteratively identify optimal pressing locations that enhance the estimation of material properties while minimizing unnecessary actions [55], [56].

Initially, we define a prior material distribution, typically modeled as a Gaussian distribution $p(e) \sim N(\mathbf{e}^*, \Sigma^*)$, where $\mathbf{e}^*$ represents the initialization of Young's modulus and Σ^* is the covariance matrix that encodes the uncertainty in the prior knowledge. At each pressing point, the robotic arm, equipped with a tactile sensor, presses the material and samples the response sequence for t times, yielding the estimated Young's modulus $\mathbf{e}_{\text{obs}}$ and an associated credibility vector $\mathbf{c}_{\text{obs}}$ with Algorithm 1. After acquiring a new observation, the posterior distribution at the $(i+1)$th update of the material properties is updated using Bayes' theorem. The $(i+1)$th updated distribution combines the (i)th updated distribution and the new observation to provide a more accurate estimate of the material properties. Assuming a Gaussian distribution, the posterior mean $\mathbf{e}_{(i+1)}$ and covariance $\mathbf{\Sigma}_{(i+1)}$ at the $(i+1)$th update are updated as follows:

$$\mathbf{\Sigma}_{(i+1)}^{-1} = \mathbf{\Sigma}_{(i)}^{-1} + \mathbf{R}^{-1} \tag{16}$$

$$\mathbf{e}_{(i+1)} = \mathbf{\Sigma}_{(i+1)}(\mathbf{\Sigma}_{(i)}^{-1}\mathbf{e}_{(i)} + \mathbf{R}^{-1}\mathbf{e}_{\text{obs}}) \tag{17}$$

where the matrix $\mathbf{R}$ is a diagonal matrix with the inverse credibility measurements as its diagonal elements. After updating the posterior distribution, multiple new sampling points are generated. The next pressing point $\mathbf{p}_{\text{next}}$ is determined by projecting onto the area with the maximum uncertainty. After sufficient iterations, an elasticity distribution could be reconstructed. This approach ensures that regions with the highest uncertainty in the estimated distribution are prioritized for pressing, thereby enhancing the efficiency of the robot-assisted sampling process.

To demonstrate the effectiveness of our sampling strategy across diverse scenarios, we evaluated it using a hemispherical model and a toy-like model with two distributed inclusions as shown in Fig. 12. Two center points with high uncertainty were identified and included in the subsequent optimization step during each update. As the sampling points were updated, more detailed information about the elasticity distributions was revealed. These results validated the capability of our sampling strategy to effectively capture the distributed inclusions.

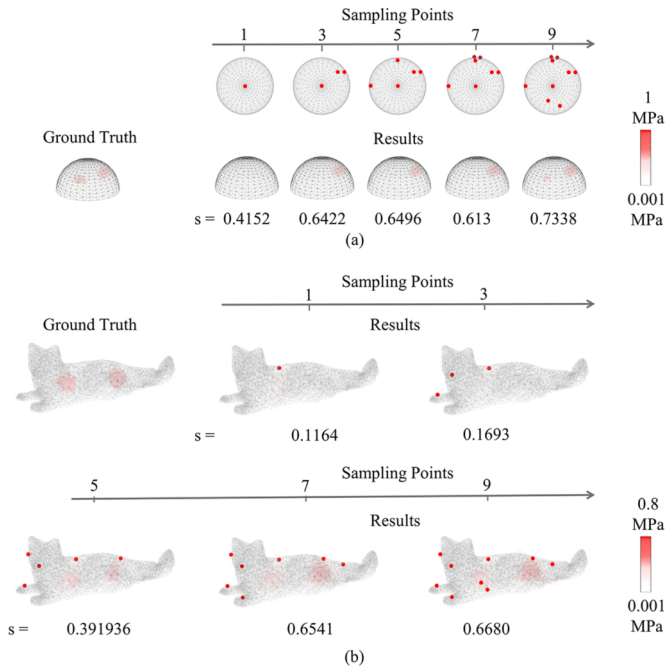

Fig. 12. Sampling demonstrations and updated elastography results based on the proposed sampling strategy. (a) Hemispherical model with two inclusions. (b) Toy-like model with two inclusions.

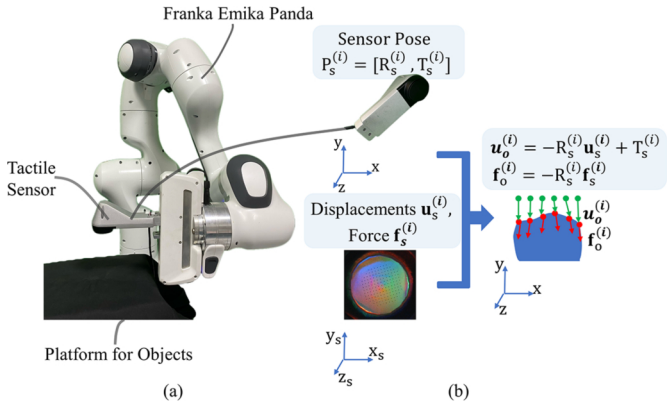

Fig. 13. Data processing in the robot-assisted experiment. (a) Robot manipulator moves the tactile sensor, positioning the object beneath the tactile surface. (b) Sampled tactile signals are transformed into the observed displacement and external force on the target object, using the global pose tracked by the manipulator.

VI. Robot-Assisted Tactile Elastography

A. Apparatus

In real-world scenarios, we built a custom data collection apparatus using a 7-DoF Franka Emika Panda robot manipulator to execute the robot-assisted experiments as displayed in Fig. 13(a). To facilitate tactile sensing and interaction, we employed a vision-based tactile sensor (Finger, Conarobot), which is a local implementation of Gelsight-like sensors, as the input device mounted as the end-effector. A total of 145 markers were strategically positioned within the tactile sensor's sensing area to detect contact force and deformation. The sensor ran at a frequency of 30 Hz, which was sufficient for the sampling requirements in our experiments.

We used three physical models to test the robot-assisted tactile elastography, including a phantom with a hard inclusion, a phantom with a spherical hole, and a real human hand with unknown geometry, as shown in Fig. 14. To build the model in Fig. 14(a) and (c), we utilized the inverted molding technique to place a hard inclusion with a diameter of 4 mm into a cubic silicone

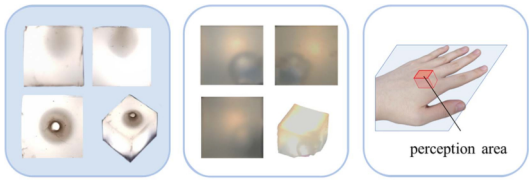

Fig. 14. Models used in the real-world experiment. (a) Soft cube model with a hard spherical inclusion. (b) Soft cube model with a hole. (c) Human hand.

model. In addition, we plucked out the spherical inclusion to get a hole at the corner of the model illustrated in Fig. 14(b). The silicone used in the model had a Young's modulus of approximately 0.2 MPa, which allowed for realistic deformation under applied pressure. The inclusion had a higher Young's modulus of approximately 2.5 GPa, providing a clear contrast in mechanical properties for the elastography measurements. To prevent the sticky surface of the phantoms from affecting the interactions, we coated the surface with a dry fine powder.

To ensure that the contact area fell entirely within the sensing region, we placed the phantom on the platform beneath the tactile sensor. We made the tactile sensor press target objects along the z-axis in the global coordinate system. We also rotated the phantom to have its different sides facing the tactile sensor to sample the tactile signals along the x- or y-direction. By monitoring the force applied to the phantom's surface through the tactile sensor, we could maintain the applied force within the desired range. In our experiment, we restrict the pressing pressure to be smaller than 0.04 MPa for a deep but safe contact. For the elastography of the hand, we kept the hand statically placed under the tactile sensor. As the hand was larger than the soft layer of the sensor, we only sampled the tactile signals from a vertical pressing test and solved for the elastography at the region beneath the contact surface.

B. Data Processing

For robot-assisted tactile elastography, we need to prepare the inputs to our computational pipeline shown in Fig. 2. We reconstruct the 3-D deformation field utilizing the vision-based tactile sensor. We adopt a calibration method for the color field similar to the approach used in Gelsight structure sensors [57], [58]. To obtain the data for color-to-gradient mapping, we press a calibration ball with a known radius (6 mm in our case) on the sensor. In addition, we press a hexagonal part on the sensor to determine the number of pixels per millimeter. For tracking the deformation and force distributions, we process the marker points by interpolating pixels around them, following [57]. This allows us to analyze the marker points' variation and capture the sensor surface's deformation.

With the known configuration of the device, we could extract the end-effector transformation $\mathbf{P}_s$ consisted of the translation $\mathbf{T}_s \in \mathbb{R}^3$ and orientation $\mathbf{R}_s \in \mathbb{R}^{3\times3}$ from the local coordinate system defined on the sensor surface to the local coordinate of the target object. In addition, the transformation was reduced to $\mathbf{d}$ when the tactile sensor moved along axes without any rotation. In this case, we converted the force and deformation field captured by the tactile sensor to the contact force and deformation of the target object by applying $\mathbf{P}_s$ to $\mathbf{x}_s$ and $\mathbf{f}_s$. Because the nodal positions at the rest mesh of the target object might not match with the markers tagged on the sensor, we interpolated for the displacement and force on the vertices of the object. With these inputs, we were ready to apply Algorithm 1 to find the elastography.

In practice, the shape of the soft layer on the tactile sensor did not conform to the contact surface of the target object. Therefore, at the beginning of the contact, only a portion of nodal tactile information on the object's surface was observable. In this case, if a vertex q on the object was not in contact with the sensor at the ith sample, we set the corresponding external force $\mathbf{f}_o^{(i)}(q)$ to zero and its deformation $\mathbf{u}_o^{(i)}$ was set according to the global transformation of the sensor. Essentially, we formed a virtual cubic region to encapsulate the target object as highlighted in Fig. 14(c) and the empty part would theoretically correspond to infinitesimal stiffness on the elastography because of the lower bound constraint e_l defined in the optimization.

C. Results

In this study, we selected ultrasound imaging as a reference due to its cost-effectiveness and accessibility, which facilitates obtaining information about internal material distributions. We presented the reconstruction results and compared the quantitative evaluation metrics with those of ultrasound images for two models as depicted in Fig. 15(a) and (b). We sliced our elasticity map and linearly adjusted the colormap to a gray scale to better compare it with the corresponding ultrasound images. We found that both the hard inclusion and the spherical hole inside the soft cube phantom could be approximately revealed by the imaging in Fig. 15(a) and (b). The stiffness of the voxels corresponding to the hole converged to the lower bound defined in the optimization problem. The ultrasound images in Fig. 15(a) and (b) show artifacts due to the shadowing effect and the posterior enhancement caused by the abnormal area. The metrics in Fig. 15(a) and (b) indicate that our results provide a 3-D distribution of the target object and achieve a relatively higher level of similarity to the ground truths compared to the ultrasound images, potentially enhancing further recognition tasks. Note that in practical experiments, the silicone replicas might exhibit an elasticity distribution that did not perfectly match the designed model due to manufacturing imperfections. This variability introduced extra discrepancies between the experimental results and the designed model.

The extension of our method to objects with unknown rest shapes was a challenging problem in our formulation. Although accurately determining the model is crucial for the global reconstruction, it may be potential to apply a simplified model to estimate the local perception roughly, as the region of interest of ultrasound imaging. Given no more prior knowledge about the human hand, we assumed the region of interest of the human hand was a cubic area below the contact surface and follows the Neo-Hookean model with a Poisson ratio 0.45 [59]. For reference, the Young's modulus of the skin, adipose tissue, muscle, and cartilage in prior work are approximately in the

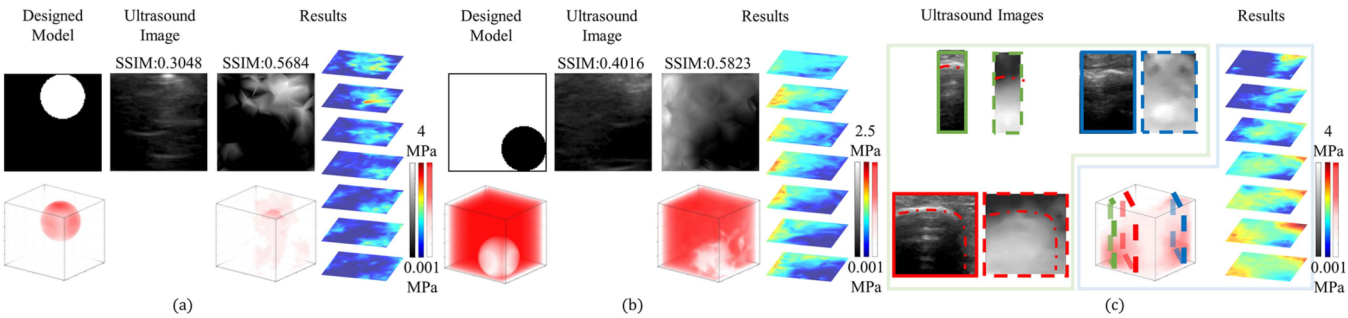

Fig. 15. Elastography results and ultrasound images of the real-world experiment. (a) and (b) Results correspond to models in Fig. 14(a) and (b). (c) Results correspond to the model in Fig. 14(c).

range of $8-700$ kPa, $0.5-5.6$ kPa, $100-400$ kPa [64], and $0.5-4.55$ MPa [65], respectively. While it was not trivial to find the interior material distribution of the hand, we opted to scan ultrasound images around a similar region as the reference for comparing our elastography results in Fig. 15(c). From the results, we observed that similar structures were highlighted as the red dashed curves in the slices of images, indicating the regions separating the bones and soft tissues. Nevertheless, restricted by the mismatches of geometry, we also found the scalar field in a few slices showed discrepancy at the shallow depth, as highlighted in the blue box in Fig. 15(c). In addition, we acknowledge that image registration across different modalities remains a challenging and unresolved issue in medical image processing. The ultrasound image of the human hand shown in Fig. 15(c) exhibits acoustic shadowing due to high-density areas. Given the absence of ground truth for the human hand, it is not suitable to quantitatively compare our results with these ultrasound images for assessments. Therefore, the ultrasound images in Fig. 15(c) are primarily used as indicative references. Overall, our results demonstrate that tactile elastography aligns well with the key structures identified in the ultrasound images during our tests.

VII. Discussion and Limitations

A. Medical Elastography Methods

By considering the observed tactile information from elasticity models, we have demonstrated the potential of tactile elastography to reveal hidden material distribution. Classic medical elastography methods, which utilize ultrasound, magnetic resonance, or optical stimulation, inspect returned signals and build models to explain the imaging results. In contrast, the proposed tactile elastography directly exploits the force and deformation on the contact surface. While existing MI solutions also attempt to generate images from haptic data, they are limited by the low-dimensional haptic signals from force sensors. Consequently, the semiheuristic images produced rely on numerous strong assumptions, which likely lead to overfitting to specific organs [22], [23], [25]. Thanks to the advanced tactile sensors, robot control, and computational resources, we strive for a more general imaging method to estimate the continuous elasticity map.

Commonly, elastography generates medical images where each pixel value is related to the elasticity of the corresponding point. As long as the image produces a meaningful scalar field to facilitate the assessment of the interior material distribution, the elastography will be acceptable in practice. For example, despite the pixels produced by ultrasound elastography are generally noisy and blurry, physicians still use it for diagnosis. In this work, we model the pixel values as Young's Modulus to indicate the hardness level of the point. Due to the nonlinearity of the simplified physical model and the sensory noise, the optimized image also exhibits noisy outputs, compared to the current techniques such as MRE or OCE. Yet, we still find the results with the color-coded hardness value display meaningful structures inside the object. In practice, users can adjust the color scale to enhance the visibility of patterns in tactile elastography. This is similar to the practical use of ultrasound imaging, in which physicians also frequently adjust the gains to better visualize the image [60]. Unlike most current medical imaging devices, vision-based tactile sensors offer advantages for tactile elastography, including low cost, easy accessibility, and operational simplicity. Another valuable finding is that interior patterns can be detected solely from partially observable haptic signals on the boundary surface. That aligns with human perception of soft objects, providing a more intuitive approach to assessing material hardness while eliminating the need for additional feature alignment often required in other imaging modalities. Moreover, the direct 3-D elasticity reconstruction sets our method apart from traditional 2-D imaging techniques. In addition, we also provide credibility measurements to help quantify the reliability of the elastography results. We believe that tactile elastography is a plausible solution for inferring invisible material distributions from subtle tactile signals through multiple pressing trials.

B. Inverse Physics Formulation

In this work, we employ inverse FEM to infer the distribution of Young's modulus as the elastography, which is one index to reflect the hardness of each point in the object. Other mechanical properties, such as Poisson's ratio or shear modulus, also encode the material features. We choose to use Young's modulus because it is sensitive to the perceived tactile signals from pressing operations. We note that Poisson's ratio is coupled with Young's modulus in many material models. Young's

modulus will not be perfectly solved if the default Poisson's ratio deviates from its ground truth. In applications involving different objects, particularly human tissues, selecting the appropriate Poisson's ratio, which varies across body parts, poses a challenge for real-world deployment due to a lack of accurate material knowledge. Furthermore, for complex soft materials, the hyperelastic model may work ineffectively, which remains an open issue. However, we also note that we do not need to perfectly reconstruct the real Young's modulus in general scenarios [61]. As elastography does not demand a strict physical interpretation of the scalar field, an approximate map of relative Young's modulus is sufficient for our purposes.

We also observe that tactile signal updates depend on both the material of the tactile sensor and the target object. Vision-based tactile sensors primarily capture the deformation of the soft layer. If the target object is too soft, the deformation of the soft layer is minimal and difficult to track visually. Conversely, if the target object is too hard, the internal material's effect on the surface deformation is negligible. In such cases, elastography can only reliably detect material properties at shallow depths. In our experiments, a soft layer with Young's modulus of 0.12 MPa works well for objects with Young's moduli ranging from 0.001 MPa to 4 MPa. Customizing the tactile sensor could enhance its sensitivity to objects with different hardness levels. In addition, the shape and size of the sensor are crucial for accurate tactile elastography. Our practical knowledge shows that a convex surface improves deformation capture by ensuring better contact [62]. The sensor size should match the object's dimensions. A sensor too small will gather insufficient data, limiting accuracy, while one too large may reduce resolution, increase noise, and complicate task execution. Larger sensors may also compromise maneuverability and precision in robotic applications. For perceiving objects of hand size, a sensor with a 1.5 cm radius may offer a balance between efficient data capture and resolution.

Postmanufacturing inconsistencies in the silicone overlay used for tactile sensors can introduce errors when applying the theoretical model to real-world scenarios. To address this, we recommend calibrating the sensor by measuring its geometry and material properties before use [63], [66]. Calibration can be performed using inverse finite element modeling based on a hyperelastic model. Once calibrated, the tactile sensor's deformation and force data can be integrated into our solver. While precise calibration remains challenging for vision-based tactile sensors [67], we found that such discrepancies do not significantly affect the core functionality of our approach. Since the focus is on capturing general material distribution characteristics rather than exact matches, our method remains effective in generating useful results. These distributions are valuable for guiding both robotic and human-assisted operations, as they adequately represent key material properties despite calibration inconsistencies.

The results still have room for improvement in terms of accuracy since we lack prior knowledge and a better initialization strategy. In our current implementation, we use a uniform distribution with a small Young's modulus value as the initialization. This choice may lead to results that are smaller than the ground truth if the convergence is insufficient. If we have more prior information about the target object, we can better initialize the stiffness distribution, which helps solve the nonlinear optimization problem. In addition, we may add regularization terms to further guide the optimization with other prior information. For instance, if we know the hardness levels of the inclusion and the tissue are close to e_c and e_t, we may add a regularization term $(e-e_c)^2(e-e_t)^2$ to prefer a binary map of e_c and e_t. Furthermore, we may add an L_1 norm on the elasticity map to encourage a smooth field except at the boundary of the inclusion. To generalize the method to a broader range of problems, we assume no prior knowledge here. What is more, assigning adaptive weights to deal with the tactile data in (7) could bring an improvement in the results as well.

As a limitation of the inverse physics formulation, the computation cost is high because the nonlinear FEM model does not have a closed solution. In this work, we use the Neo-Hookean model because it is more suitable for capturing the general deformation of the soft tissue, whereas linear material models are only effective for subtle deformation. As a first step in extracting elastography from tactile signals, we anticipate future work to reduce the computation cost by introducing a dedicated initialization scheme with the Monte Carlo method. More engineering steps such as the adoption of advanced numerical solvers, parallel computation, and more powerful computation hardware can further reduce the computation time. Moreover, formulating data-driven surrogate models is another option to solve the inverse problem. However, data-driven approaches are at the cost of preparing high-quality training data. We expect further studies to explore learning-based methods for improving tactile elastography, while the proposed physics-based model could serve as an appropriate baseline for potential future work.

VIII. Conclusion

We work on the challenging problem of imaging the interior material distribution under the skin of the object. By exploiting the tactile information from active contact trials, we introduce an inverse physics model to solve for the 3-D elasticity distribution. Compared with the 2-D tactile images sampled on the surface, tactile elastography provides a more intuitive approach for operators to understand the interior material distribution of objects. In the experiments, we discuss the credibility of varying elasticities at varying depths under different external forces and observe the influence of different sampling data. We also show the applications of tactile elastography in depth estimation and shape recognition of invisible hard inclusions. Furthermore, we showcase the capability of robot-assisted tactile elastography in imaging the interior materials of real-world objects using tactile cues.

In this work, we use a 7-DoF robot manipulator to actuate and locate the tactile sensor. This setup constrains the workspace of the tactile sensor. To produce elastography on larger models with complex shapes, a larger workspace for more flexible and intelligent active contact operations is required. For future work, a motion capture system could be employed to track the global motion of the tactile sensor, enabling the perception of objects from varying directions with a hand-held sampling strategy. It is also interesting to explore more advanced pressing policies to

safely sample the haptic information for tactile elastography. As the deployment of tactile sensors grows, there is significant potential to adopt tactile elastography as the offline precomputation stage in robotic manipulation tasks involving soft objects, such as precise grasping and shaping. In addition, we anticipate further exploration of tactile elastography's medical applications, particularly in remote palpation diagnostics.

Acknowledgment

The authors would like to thank the IEC for the ethical approval provided for Clinical Research of Zhongda Hospital, Affiliated to Southeast University.

References

[1] Y. Wang, C. Nguyen, R. Srikanchana, Z. Geng, and M. T. Freedman, "Tactile mapping of palpable abnormalities for breast cancer diagnosis," in *Proc. IEEE Int. Conf. Robot. Automat.*, 1999, vol. 2, pp. 1305–1309.

[2] P. S. Wellman, E. P. Dalton, D. Krag, K. A. Kern, and R. D. Howe, "Tactile imaging of breast masses: First clinical report," *Arch. Surg.*, vol. 136, no. 2, pp. 204–208, 2001.

[3] L. Han, A. Noble, and M. Burcher, "The elastic reconstruction of soft tissues," in *Proc. IEEE Int. Symp. Biomed. Imag.*, 2002, pp. 1035–1038.

[4] K. Sangpradit, H. Liu, P. Dasgupta, K. Althoefer, and L. D. Seneviratne, "Finite-element modeling of soft tissue rolling indentation," *IEEE Trans. Biomed. Eng.*, vol. 58, no. 12, pp. 3319–3327, Dec. 2011.

[5] B. Ahn, Y. Kim, C. K. Oh, and J. Kim, "Robotic palpation and mechanical property characterization for abnormal tissue localization," *Med. Biol. Eng. Comput.*, vol. 50, pp. 961–971, 2012.

[6] B. Xiao et al., "Depth estimation of hard inclusions in soft tissue by autonomous robotic palpation using deep recurrent neural network," *IEEE Trans. Automat. Sci. Eng.*, vol. 17, no. 4, pp. 1791–1799, Oct. 2020.

[7] A. Davis, K. L. Bouman, J. G. Chen, M. Rubinstein, F. Durand, and W. T. Freeman, "Visual vibrometry: Estimating material properties from small motion in video," in *Proc. IEEE Conf. Comput. Vis. Pattern Recognit.*, 2015, pp. 5335–5343.

[8] B. T. Feng, A. C. Ogren, C. Daraio, and K. L. Bouman, "Visual vibration tomography: Estimating interior material properties from monocular video," in *Proc. IEEE/CVF Conf. Comput. Vis. Pattern Recognit.*, 2022, pp. 16210–16219.

[9] T. R. Nelson and D. H. Pretorius, "Three-dimensional ultrasound imaging," *Ultrasound Med. Biol.*, vol. 24, no. 9, pp. 1243–1270, 1998.

[10] H. Maekawa, K. Tanie, K. Komoriya, M. Kaneko, C. Horiguchi, and T. Sugawara, "Development of a finger-shaped tactile sensor and its evaluation by active touch," in *Proc. IEEE Int. Conf. Robot. Automat.*, 1992, pp. 1327–1334.

[11] C. Chi, X. Sun, N. Xue, T. Li, and C. Liu, "Recent progress in technologies for tactile sensors," *Sensors*, vol. 18, no. 4, 2018, Art. no. 948.

[12] S. Zhang et al., "Hardware technology of vision-based tactile sensor: A review," *IEEE Sensors J.*, vol. 22, no. 22, pp. 21410–21427, Nov. 2022.

[13] J. Ophir et al., "Elastography: Imaging the elastic properties of soft tissues with ultrasound," *J. Med. Ultrasonics*, vol. 29, pp. 155–171, 2002.

[14] Z. Guo, S. You, X. Wan, and N. Bićanić, "A FEM-based direct method for material reconstruction inverse problem in soft tissue elastography," *Comput. Structures*, vol. 88, no. 23, pp. 1459–1468, 2010.

[15] J.-L. Gennisson, T. Deffieux, M. Fink, and M. Tanter, "Ultrasound elastography: Principles and techniques," *Diagn. Interventional Imag.*, vol. 94, no. 5, pp. 487–495, 2013.

[16] R. B. Buxton, *Introduction to Functional Magnetic Resonance Imaging: Principles and Techniques*. Cambridge, U.K.: Cambridge Univ. Press, 2009.

[17] Y. K. Mariappan, K. J. Glaser, and R. L. Ehman, "Magnetic resonance elastography: A review," *Clin. Anatomy*, vol. 23, no. 5, pp. 497–511, 2010.

[18] D. Huang et al., "Optical coherence tomography," *Science*, vol. 254, no. 5035, pp. 1178–1181, 1991.

[19] J. Ophir et al., "Elastography: Ultrasonic estimation and imaging of the elastic properties of tissues," *Proc. Inst. Mech. Engineers, Part H: J. Eng. Med.*, vol. 213, no. 3, pp. 203–233, 1999.

[20] R. A. Leitgeb, R. M. Werkmeister, C. Blatter, and L. Schmetterer, "Doppler optical coherence tomography," *Prog. Retinal Eye Res.*, vol. 41, pp. 26–43, 2014.

[21] X. Liang, V. Crecea, and S. A. Boppart, "Dynamic optical coherence elastography: A review," *J. Innov. Opt. Health Sci.*, vol. 3, no. 04, pp. 221–233, 2010.

[22] V. Egorov, S. Ayrapetyan, and A. P. Sarvazyan, "Prostate mechanical imaging: 3D image composition and feature calculations," *IEEE Trans. Med. Imag.*, vol. 25, no. 10, pp. 1329–1340, Oct. 2006.

[23] V. Egorov and A. P. Sarvazyan, "Mechanical imaging of the breast," *IEEE Trans. Med. Imag.*, vol. 27, no. 9, pp. 1275–1287, Sep. 2008.

[24] A. Sarvazyan and V. Egorov, "Mechanical imaging—A technology for 3D visualization and characterization of soft tissue abnormalities: A review," *Curr. Med. Imag.*, vol. 8, no. 1, pp. 64–73, 2012.

[25] L. G. Olson et al., "An inverse problem approach to stiffness mapping for early detection of breast cancer: Tissue phantom experiments," *Inverse Problems Sci. Eng.*, vol. 27, no. 7, pp. 1006–1037, 2019.

[26] B. Wang, L. Wu, K. Yin, U. M. Ascher, L. Liu, and H. Huang, "Deformation capture and modeling of soft objects," *ACM Trans. Graph.*, vol. 34, no. 4,, 2015, Art. no. 94.

[27] H. Xu, Y. Li, Y. Chen, and J. Barbič, "Interactive material design using model reduction," *ACM Trans. Graph.*, vol. 34, no. 2, pp. 1–14, 2015.

[28] R. Ambrus, V. Guizilini, N. Kuppuswamy, A. Beaulieu, A. Gaidon, and A. Alspach, "Monocular depth estimation for soft visuotactile sensors," in *Proc. IEEE 4th Int. Conf. Soft Robot.*, 2021, pp. 643–649.

[29] H.-J. Huang, X. Guo, and W. Yuan, "Understanding dynamic tactile sensing for liquid property estimation," in *Proc. Robot. Sci. Syst.*, New York City, NY, USA, Jun. 2022, doi: 10.15607/RSS.2022.XVIII.072.

[30] W. Yuan, C. Zhu, A. Owens, M. A. Srinivasan, and E. H. Adelson, "Shape-independent hardness estimation using deep learning and a GelSight tactile sensor," in *Proc. IEEE Int. Conf. Robot. Automat.*, 2017, pp. 951–958.

[31] W. Yuan, S. Wang, S. Dong, and E. Adelson, "Connecting look and feel: Associating the visual and tactile properties of physical materials," in *Proc. IEEE Conf. Comput. Vis. Pattern Recognit.*, 2017, pp. 4494–4502.

[32] X. Jia, R. Li, M. A. Srinivasan, and E. H. Adelson, "Lump detection with a GelSight sensor," in *Proc. IEEE World Haptics Conf.*, 2013, pp. 175–179.

[33] E. Donlon, S. Dong, M. Liu, J. Li, E. Adelson, and A. Rodriguez, "GelSlim: A high-resolution, compact, robust, and calibrated tactile-sensing finger," in *Proc. IEEE/RSJ Int. Conf. Intell. Robots Syst.*, 2018, pp. 1927–1934.

[34] I. H. Taylor, S. Dong, and A. Rodriguez, "GelSlim 3.0: High-resolution measurement of shape, force and slip in a compact tactile-sensing finger," in *Proc. Int. Conf. Robot. Automat.*, 2022, pp. 10781–10787.

[35] T. Yamamoto, B. Vagvolgyi, K. Balaji, L. L. Whitcomb, and A. M. Okamura, "Tissue property estimation and graphical display for teleoperated robot-assisted surgery," in *Proc. IEEE Int. Conf. Robot. Automat.*, 2009, pp. 4239–4245.

[36] A. L. Trejos, J. Jayender, M. Perri, M. D. Naish, R. V. Patel, and R. Malthaner, "Robot-assisted tactile sensing for minimally invasive tumor localization," *Int. J. Robot. Res.*, vol. 28, no. 9, pp. 1118–1133, 2009.

[37] H. Kim, S. Choi, and W. K. Chung, "Feasibility of a novel indicator for lump detection using contact pressure distribution," in *Proc. IEEE/RSJ Int. Conf. Intell. Robots Syst.*, 2015, pp. 2111–2117.

[38] Z. Zhou et al., "Methods to recognize depth of hard inclusions in soft tissue using ordinal classification for robotic palpation," *IEEE Trans. Instrum. Meas.*, vol. 71, 2022, Art. no. 2516512.

[39] S. Zhang, "High-speed 3D shape measurement with structured light methods: A review," *Opt. Lasers Eng.*, vol. 106, pp. 119–131, 2018.

[40] M. A. Hopcroft, W. D. Nix, and T. W. Kenny, "What is the Young's modulus of silicon?," *J. Microelectromech. Syst.*, vol. 19, no. 2, pp. 229–238, 2010.

[41] Z. Wang, A. C. Bovik, H. R. Sheikh, and E. P. Simoncelli, "Image quality assessment: From error visibility to structural similarity," *IEEE Trans. Image Process.*, vol. 13, no. 4, pp. 600–612, Apr. 2004.

[42] D. Poobathy and M. Chezian, "Edge detection operators: Peak signal to noise ratio based comparison," *Int. J. Image, Graph. Signal Process.*, vol. 6, pp. 55–61, 2014.

[43] T. Chai and R. R. Draxler, "Root mean square error (RMSE) or mean absolute error (MAE)? – Arguments against avoiding RMSE in the literature," *Geoscientific Model Develop.*, vol. 7, pp. 1247–1250, 2014.

[44] U. Sara, M. Akter, and M. S. Uddin, "Image quality assessment through FSIM, SSIM, MSE and PSNR — A comparative study," *J. Comput. Commun.*, vol. 7, no. 3, pp. 8–18, 2019.

[45] S. Ahmed, U. Kamal, and M. K. Hasan, "DSWE-Net: A deep learning approach for shear wave elastography and lesion segmentation using single push acoustic radiation force," *Ultrasonics*, vol. 110, 2021, Art. no. 106283.

[46] F. Dai et al., "B-mode ultrasound to elastography synthesis using multiscale learning," *Ultrasonics*, vol. 138, 2024, Art. no. 107268.

[47] G. Kim et al., "A new voxelization strategy in compressed-sensing (CS)-based iterative CT reconstruction for reducing computational cost: Simulation and experimental studies," *J. Med. Biol. Eng.*, vol. 38, pp. 129–137, 2018.
[48] P. Maken and A. Gupta, "2D-to-3D: A review for computational 3D image reconstruction from X-ray images," *Arch. Comput. Methods Eng.*, vol. 30, no. 1, pp. 85–114, 2023.
[49] C. Papadacci, E. A. Bunting, and E. E. Konofagou, "3D quasi-static ultrasound elastography with plane wave in vivo," *IEEE Trans. Med. Imag.*, vol. 36, no. 2, pp. 357–365, Feb. 2017.
[50] D. Fovargue, D. Nordsletten, and R. Sinkus, "Stiffness reconstruction methods for MR elastography," *NMR Biomed.*, vol. 31, no. 10, 2018, Art. no. e3935.
[51] L. Robert, F. Nazaret, T. Cutard, and J.-J. Orteu, "Use of 3-D digital image correlation to characterize the mechanical behavior of a fiber reinforced refractory castable," *Exp. Mechan.*, vol. 47, no. 6, pp. 761–773, 2007.
[52] J. C. Gwilliam, Z. Pezzementi, E. Jantho, A. M. Okamura, and S. Hsiao, "Human vs. robotic tactile sensing: Detecting lumps in soft tissue," in *Proc. IEEE Haptics Symp.*, 2010, pp. 21–28.
[53] J. Dai, Y. Li, K. He, and J. Sun, "R-FCN: Object detection via region-based fully convolutional networks," in *Proc. Adv. Neural Inf. Process. Syst.*, 2016, vol. 29, pp. 379–387.
[54] P. H. S. Torr, "Bayesian model estimation and selection for epipolar geometry and generic manifold fitting," *Int. J. Comput. Vis.*, vol. 50, pp. 35–61, 2002.
[55] G. Rizzi, J. J. Chung, A. Gawel, L. Ott, M. Tognon, and R. Siegwart, "Robust sampling-based control of mobile manipulators for interaction with articulated objects," *IEEE Trans. Robot.*, vol. 39, no. 3, pp. 1929–1946, Jun. 2023.
[56] R. Platt, F. Permenter, and J. Pfeiffer, "Using Bayesian filtering to localize flexible materials during manipulation," *IEEE Trans. Robot.*, vol. 27, no. 3, pp. 586–598, Jun. 2011.
[57] S. Wang, Y. She, B. Romero, and E. Adelson, "GelSight wedge: Measuring high-resolution 3D contact geometry with a compact robot finger," in *Proc. IEEE Int. Conf. Robot. Automat.*, 2021, pp. 6468–6475.
[58] W. Li et al., "L^3 F-TOUCH: A wireless GelSight with decoupled tactile and three-axis force sensing," *IEEE Robot. Autom. Lett.*, vol. 8, no. 8, pp. 5148–5155, Aug. 2023.
[59] H. Kim, L. Yoo, A. Shin, and J. L. Demer, "Determination of ratio of bovine extraocular muscle by computed X-ray tomography," *BioMed Res. Int.*, vol. 2013, no. 1, 2013, Art. no. 197479.
[60] Y. Wang, M. Koen, and D. Ma, "Low-noise CMOS TCG amplifier with adaptive gain control for ultrasound imaging receivers," *IEEE Trans. Circuits Syst. II: Exp. Briefs*, vol. 58, no. 1, pp. 26–30, Jan. 2011.
[61] G.-Y. Li and Y. Cao, "Mechanics of ultrasound elastography," *Proc. Roy. Soc. A: Math., Phys. Eng. Sci.*, vol. 473, no. 2199, 2017, Art. no. 20160841.
[62] A. Padmanabha, F. Ebert, S. Tian, R. Calandra, C. Finn, and S. Levine, "OmniTact: A multi-directional high-resolution touch sensor," in *Proc. IEEE Int. Conf. Robot. Automat.*, 2020, pp. 618–624.
[63] D. Ma, E. Donlon, S. Dong, and A. Rodriguez, "Dense tactile force estimation using GelSlim and inverse FEM," in *Proc. Int. Conf. Robot. Automat.*, 2019, pp. 5418–5424.
[64] J. T. Iivarinen, R. K. Korhonen, P. Julkunen, and J. S. Jurvelin, "Experimental and computational analysis of soft tissue stiffness in forearm using a manual indentation device," *Med. Eng. Phys.*, vol. 33, no. 10, pp. 1245–1253, 2011.
[65] W. Kabir, C. D. Bella, P. F. Choong, and C. D. O'Connell, "Assessment of native human articular cartilage: A biomechanical protocol," *Cartilage*, vol. 13, no. 2_suppl, pp. 427S–437S, 2021.
[66] K. Sato, K. Kamiyama, H. Nii, N. Kawakami, and S. Tachi, "Measurement of force vector field of robotic finger using vision-based haptic sensor," in *Proc. IEEE/RSJ Int. Conf. Intell. Robots Syst.*, 2008, pp. 488–493.
[67] S. K. Melly, L. Liu, Y. Liu, and J. Leng, "A review on material models for isotropic hyperelasticity," *Int. J. Mech. Syst. Dyn.*, vol. 1, no. 1, pp. 71–88, 2021.

Yichen Xiang received the B.S. degree in instrument science and engineering in 2021 from Southeast University, Nanjing, China, where she is currently working toward the Ph.D. degree in robotics with the Jiangsu Key Lab of Remote Measurement and Control, School of Instrument Science and Engineering.

Her research interests include haptics, tactile, and robotics.

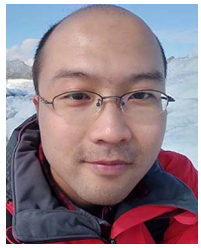

Lifeng Zhu (Member, IEEE) received the Ph.D. degree in computer science from Peking University, Beijing, China, in 2012.

He is currently a Professor with the Department of Instrument Science and Engineering, Southeast University, Nanjing, China. His research interests include visual computing, human computer interaction, robotics, particularly shape modeling, physical simulation, and their applications in medical science and fabrication.

Aiguo Song (Senior Member, IEEE) received the B.S. degree in automatic control and the M.S. degree in measurement and control from the Nanjing University of Aeronautics and Astronautics, Nanjing, China, in 1990 and 1993, respectively, and the Ph.D. degree in measurement and control from Southeast University, Nanjing, China, in 1996.

He is currently a Professor with the Department of Instrument Science and Engineering, Southeast University. His research interests include haptic display, robot tactile sensor, and telerehabilitation robot.

Dr. Song is a Member of the Chinese Instrument Association.

Yongjie Jessica Zhang received the B.Eng. degree in automotive engineering in 1996 and the M.Eng. degree in engineering mechanics in 1999 from Tsinghua University, Beijing, China, the M.Eng. degree in aerospace engineering and engineering mechanics in 2002, and the Ph.D. degree in computational engineering and sciences in 2005 from the Institute for Computational Engineering and Sciences, the University of Texas at Austin, Austin, TX, USA.

She is the George Tallman Ladd and Florence Barrett Ladd Professor of mechanical engineering with Carnegie Mellon University, Pittsburgh, PA, USA, with a courtesy appointment in biomedical engineering. Her research interests include computational geometry, isogeometric analysis, finite element method, data-driven modeling, image processing, and mesh generation.